THE ASTROPHYSICAL JOURNAL, 535:1047–1065, 2000 June 1

TIME VARIABILITY OF THE "QUIET" SUN OBSERVED WITH *TRACE*. II. PHYSICAL PARAMETERS, TEMPERATURE EVOLUTION, AND ENERGETICS OF EXTREME-ULTRAVIOLET NANOFLARES

MARKUS J. ASCHWANDEN, TED D. TARBELL, RICHARD W. NIGHTINGALE, CAROLUS J. SCHRIJVER, AND ALAN TITLE
Lockheed Martin Advanced Technology Center, Solar and Astrophysics Laboratory, Department L941, Building 252, 3251 Hanover Street, Palo Alto, CA 94304; aschwanden@lmsal.com

CHARLES C. KANKELBORG AND PIET MARTENS
Department of Physics, Montana State University–Bozeman, P.O. Box 173840, Bozeman, MO 59717

AND

HARRY P. WARREN
Harvard-Smithsonian Center for Astrophysics, Mail Stop 58, 60 Garden Street, Cambridge, MA 02138
Received 1999 July 27; accepted 2000 January 4

ABSTRACT

We present a detailed analysis of the geometric and physical parameters of 281 EUV nanoflares, simultaneously detected with the *TRACE* telescope in the 171 and 195 Å wavelengths. The detection and discrimination of these flarelike events is detailed in the first paper in this series. We determine the loop length l, loop width w, emission measure EM, the evolution of the electron density $n_e(t)$ and temperature $T_e(t)$, the flare decay time τ_{decay}, and calculate the radiative loss time τ_{loss}, the conductive loss time τ_{cond}, and the thermal energy E_{th}. The findings are as follows: (1) EUV nanoflares in the energy range of 10^{24}–10^{26} ergs represent miniature versions of larger flares observed in soft X-rays (SXR) and hard X-rays (HXR), scaled to lower temperatures ($T_e \lesssim 2$ MK), lower densities ($n_e \lesssim 10^9$ cm^{-3}), and somewhat smaller spatial scales ($l \approx 2$–20 Mm). (2) The cooling time τ_{decay} is compatible with the radiative cooling time τ_{rad}, but the conductive cooling timescale τ_{cond} is about an order of magnitude shorter, suggesting repetitive heating cycles in time intervals of a few minutes. (3) The frequency distribution of thermal energies of EUV nanoflares, $N(E) \approx 10^{-46}(E/10^{24})^{-1.8}$ (s^{-1} cm^{-2} ergs^{-1}) matches that of SXR microflares in the energy range of 10^{26}–10^{29}, and exceeds that of nonthermal energies of larger flares observed in HXR by a factor of 3–10 (in the energy range of 10^{29}–10^{32} ergs). Discrepancies of the power-law slope with other studies, which report higher values in the range of $a = 2.0$–2.6 (Krucker & Benz; Parnell & Jupp), are attributed to methodical differences in the detection and discrimination of EUV microflares, as well as to different model assumptions in the calculation of the electron density. Besides the insufficient power of nanoflares to heat the corona, we find also other physical limits for nanoflares at energies $\lesssim 10^{24}$ ergs, such as the area coverage limit, the heating temperature limit, the lower coronal density limit, and the chromospheric loop height limit. Based on these quantitative physical limitations, it appears that coronal heating requires other energy carriers that are not luminous in EUV, SXR, and HXR.

Subject headings: Sun: chromosphere — Sun: corona — Sun: transition region — Sun: UV radiation

1. INTRODUCTION

Three major mechanisms have been proposed to heat the solar corona: (1) dissipation of Alfvén waves, (2) resistive dissipation of DC electric currents, and (3) MHD turbulence (e.g., see review by Zirker 1993). The second mechanism, resistive dissipation of electric currents, is thought to occur, e.g., in current sheets during magnetic reconnection processes. Magnetic reconnection processes certainly occur in the corona, there is mounting evidence from recent spacecraft observations such as *Yohkoh*, *SOHO*, and *TRACE*, but they are also thought to occur in the transition region and chromosphere (e.g., Litvinenko 1999). A key question is whether magnetic reconnection processes provide us sufficiently unambiguous observational signatures that allow us to detect, identify, and quantify the energy input and to test its efficiency for coronal heating. Parker (1988) suggested that the solar corona could be heated by dissipation of many tangential discontinuities arising spontaneously in the coronal magnetic field that is stirred by random photospheric footpoint motions. This theory stimulated numerous searches for observational signatures of nanoflares. In this study we present a rigorous and comprehensive analysis of a 1 hr data set obtained with the *TRACE* telescope from the *quiet Sun*, which exhibits copious small-scale phenomena that energetically may be considered as nanoflare signatures in EUV wavelengths.

Let us briefly highlight some previous observational work on microflare (10^{27}–10^{30} ergs) or nanoflare (10^{24}–10^{27} ergs) detection. Lin et al. (1984) reported microflares at greater than 20 keV hard X-rays with energies of $\approx 10^{27}$ ergs, exhibiting bursts with 1–2 s time structures over periods of 5–100 s. Apparently such small energy releases produce sufficiently strong electric fields to accelerate electrons to nonthermal (>20 keV) energies. Porter et al. (1987) detected small-scale brightenings in EUV (C IV) that coincided with small magnetic bipoles, which were interpreted as microflares and drivers of spicules. Dere, Bartoe, & Brueckner (1989) and Dere et al. (1991) report on explosive events in EUV (C IV), which were interpreted, owing to their Doppler shift, in terms of plasma jets emerging from cancelling reconnection events, but they seem also (like Porter's microflares) not to play a major role for coronal heating owing to their low (transition region) temperature (around 0.1 MK). With a correlative study, Porter, Fontenla, &

Simnett (1995) demonstrated that explosive events seen in EUV (C IV) had counterparts in soft X-rays (SXR) and thus should be considered as microflares. Statistics of microflares in active regions, called *transient brightenings* in SXR, have been studied by Shimizu et al. (1992), Shimizu (1997), and Shimizu & Tsuneta (1997), demonstrating that these smallest detected SXR signatures with energies in the range of $\approx 10^{27}$–10^{29} ergs represent miniature flares, regarding their physical parameters, and also with respect to the similarity of their frequency distribution with larger flares (with energies of $\approx 10^{28}$–10^{32} ergs) detected in hard X-rays (HXR) (Crosby, Aschwanden, & Dennis 1993). Statistics on the smallest HXR microflares has been gathered by Biesecker, Ryan, & Fishman (1994), probably down to an energy level of $\gtrsim 10^{27}$ ergs. While the occurrence frequency and energetics of all these microflaring phenomena in active regions were found not to be powerful enough to heat the solar corona, new studies concentrated on the quiet Sun, away from active regions, where the background flux and telescope stray light is weaker, and thus microflares should be detectable with better contrast. Statistics of EUV microflares in the quiet Sun, using *SOHO*/EIT (Krucker & Benz 1998) and *TRACE* data (Parnell & Jupp 2000) came up for the first time with power-law slopes of $a \approx 2.0$–2.6 in the frequency distribution of energies, suggesting that the distribution at smaller energies could sufficiently diverge above the critical value of $a = 2$ (Hudson 1991), to meet the coronal heating requirement. Benz & Krucker (1998) estimated that the sum of all significant EUV brightenings observed in EIT 171/195 Å images could account for up to $\approx 50\%$ of the coronal heating requirement. Benz & Krucker (1999) demonstrated also that some of the largest EUV brightenings show temporal correlations and relative time delays in He II, C II, C IV, O V, Fe IX/X, Fe XI, and in microwave emission as expected for flare events. These observations thus corroborate that flarelike processes extend from large flares ($E \approx 10^{32}$ ergs) now over ≈ 7 orders of magnitude down to the nanoflare regime (at $\gtrsim 10^{25}$ ergs). The occurrence rate of nanoflares is still controversial because a similar statistical study reports a significantly flatter slope in the frequency distribution ($a = -1.35$ for flare events detected with *SOHO*/EIT 195 Å; Berghmans, Clette, & Moses 1998) than the high values ($a = 2.0$–2.6) determined by Krucker & Benz (1998) and Parnell & Jupp (2000). The value of this power-law slope, however, represents the most decisive criterion as to whether nanoflares have sufficient power to heat the solar corona.

In this study we take advantage of the unprecedented high spatial resolution of the *TRACE* instrument (with pixel size of 0.″5) to analyze the physical parameters of EUV nanoflares. The statistics of EUV brightenings and the discrimination of flarelike events is described in Paper I (Aschwanden et al. 2000). In this second part (Paper II) we analyze the geometric parameters of 281 flarelike events (§ 2.1), their physical parameters (§ 2.2), their temperature evolution (§ 2.3), and their density evolution and radiative cooling (§ 2.4). We discuss scaling laws between EUV nanoflares, SXR microflares, and HXR flares (§ 3.1) and compare their frequency distributions (§ 3.2). We explore then the scaling of flare parameters into the picoflare regime (§ 3.3) and evaluate area coverage limits for nano- and picoflares (§ 3.4). Finally we evaluate the energy balance in the observed EUV nanoflares (§ 3.5), their globally averaged energy output (§ 3.6), and their energy budget with respect to the coronal heating requirement (§ 3.7). Conclusions are enumerated in § 4.

2. DATA ANALYSIS OF MICROFLARES

We analyze the geometric and physical parameters of all flarelike events detected with the *TRACE* telescope (Handy et al. 1999) at 195 Å during the orbit of 1998 February 17, 0215–0300 UT. Using the automated flare criterion described in § 6.1 of Paper I (with the requirement that all the temporal, spatial, and dynamic cross-correlation coefficients between the 171 and 195 Å data have a value of ccc > 0.5), we detected 281 flarelike events (Table 3 in Paper I), of which 83% (222 events) have also been independently classified as flare events by visual criteria.

2.1. *Geometric Parameters*

The spatial distribution of the detected 281 flarelike events (also called microflares or nanoflares in the following) are shown in Figure 1. The size of each microflare is indicated with an ellipsoidal area that encompasses all macropixels (with a size of 2″) with significant ($\geq 3\ \sigma$) and near-coincident (within ± 2 minutes) time variability associated with a particular microflare. The 195 Å map in Figure 1 shows that the spatial distribution of microflares (observed over a time interval of 45 minutes) is not randomly distributed but tends to be clustered in areas near active regions.

The 195 Å EUV brightness changes $\Delta F(x, y)$ of 20 individual events are shown in Figure 2, including a representative set of the brightest detected microflares. The gray-scale representations and contour plots shown in Figure 2 represent difference images $\Delta F(x, y) = F(x, y, t = t_{\rm peak}) - F(x, y, t = t_{\rm min})$, where the images at the peak time $t_{\rm peak}$ and minimum time $t_{\rm min}$ are each averaged over five time steps to improve the signal-to-noise ratio. Note that the ellipse boundaries confine only those macropixels with near-simultaneous time variability, which do not necessarily coincide with the areas of enhanced brightness in the difference images, because activities in adjacent flare loops may peak at different times. If flare loops have a temporal peak $\gtrsim 4$ minutes apart, they were considered as different microflares (see event definition in § 5.1 of Paper I).

While microflare geometries were mainly characterized with two-dimensional models (i.e., with the projected area) in previous studies (e.g., Krucker & Benz 1998; Parnell & Jupp 2000), we attempt here to apply a simple three-dimensional model of microflare loops. The examples in Figure 2 illustrate that most of the microflares show some elongated structures with well-defined boundaries, which can generally be interpreted as flare loops, judging from their typical spatial scales. The spatial scales of the confining ellipses cover a range of $a \approx 3$–20 Mm for the major axis and a range of $b \approx 1.5$–10 Mm for the minor axis (§ 5.3 in Paper I). However, the area of variable pixels does not always fill the elliptical boundaries with a filling factor of unity. Often, in particular when a microflare consists of multiple loop structures, or when the projection of a curved loop is not straight, only a fraction $q_{\rm ell}$ of the confining ellipse is filled. In the ellipse fitting procedure (§ 5.3 in Paper I) we determined also roughly the area A of each variability event, by summing the pixel areas of all N variable macropixels per event, i.e., $A = \sum_{i=1}^{N} \Delta x\ \Delta y$. Based on the geometric area $A_{\rm ell} = (\pi/4)ab$ of an ellipse with major axis a

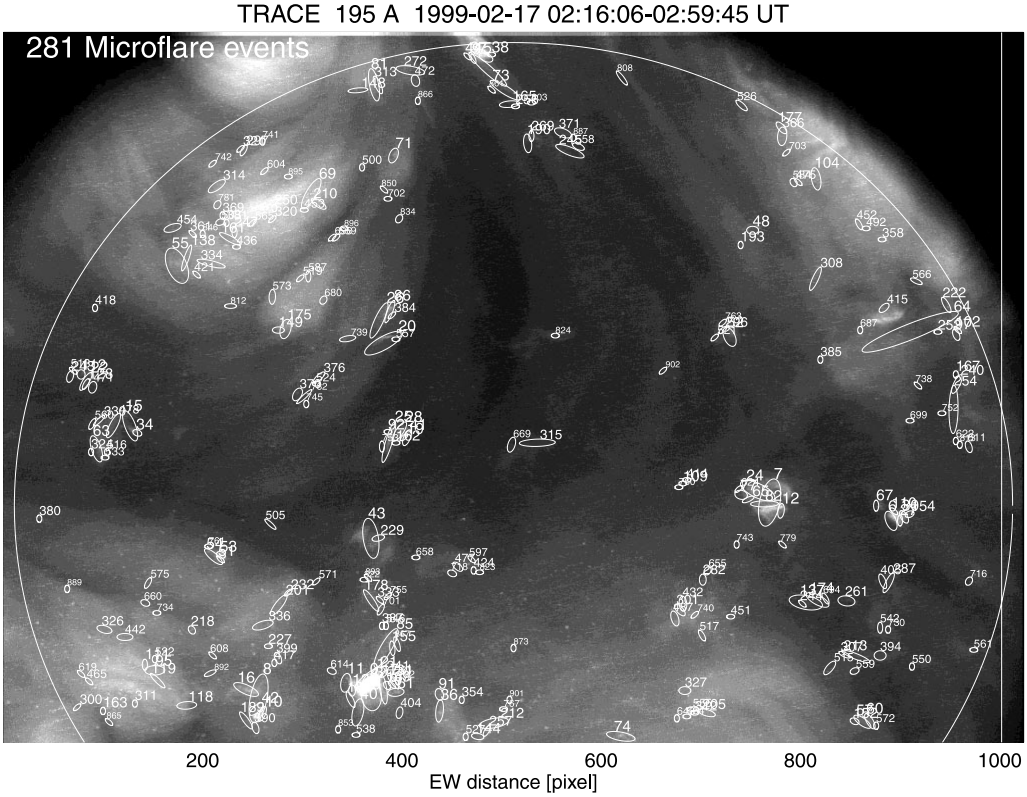

FIG. 1.—This synthesized *TRACE* 195 Å image is summed from 22 images recorded during 1999 February 17 02:16:06–02:59:45 UT. The circle encompasses the analyzed field of view with a diameter of $\approx 8'$. The numbered ellipses mark 281 flarelike events that fulfill the flare criterion (see Paper I) of 901 EUV brightening events. The geometric size and orientation of the ellipses is on scale, containing all simultaneously varying pixels of a flare event.

and minor axis b, we can define an ellipse area filling factor

$$q_{\rm ell} = \frac{A}{A_{\rm ell}} = \frac{\sum_{i=1}^{N} \Delta x \, \Delta y}{(\pi/4)ab} \, . \tag{1}$$

The relation between the projected area of a semicircular loop (with radius r and width w) and a confining ellipse (with axes a and b) is visualized in Figure 3 (*bottom*). An approximate estimate of the projected loop length l can be obtained by setting the major ellipse axis equal to the projected loop length l, while the loop equivalent width w can be estimated by dividing the minor ellipse axis by the filling factor, i.e.,

$$l \approx a \tag{2}$$

$$w \approx b q_{\rm ell} \, . \tag{3}$$

This method allows us to estimate the most essential geometric parameters l and w without fitting a full three-dimensional loop model, which could not be properly performed for most of the microflares anyway, owing to their poor signal-to-noise ratio and unsharp spatio-temporal separation. Although the three-dimensional geometry cannot accurately be determined for small-scale microflares, we aim to correct at least for the finite thickness of the chromosphere, which contains a substantial segment of the flare loop when its size becomes comparable with the height of the chromosphere. This is sketched in Figure 3 (*top*), where the flare loop footpoints up to a height of $h_{\rm Ch} \approx 2.5$ Mm are immersed in the chromosphere. The physical conditions in this chromospheric segment are entirely different from the coronal part owing to the higher density, pressure, and magnetic field. The resulting temperature drop and high conductive loss rate in and below the transition region make it unlikely to observe EUV emission in the 1.0–1.5 MK temperature range, so that we do not expect to see this chromospheric loop segments in 171 and 195 Å wavelengths. If a semicircular loop is characterized with a projected length l (above the chromosphere) and width w, the loop radius r amounts to

$$r = \sqrt{(l/2)^2 + h_{\rm Ch}^2} - w/2 \tag{4}$$

(see Fig. 3 [*top*]). The full volume $V_{\rm loop}$ of the semicircular loop cylinder is

$$V_{\rm loop} = \pi r \times \pi \left(\frac{w}{2}\right)^2 = \frac{\pi^2 r w^2}{4} \, , \tag{5}$$

while the observed volume with luminous EUV emission (in the loop segment above the chromosphere) is

$$V_{\rm EUV} = V_{\rm loop} \left[1 - \frac{2}{\pi} \arctan \left(\frac{h_{\rm Ch}}{l/2} \right) \right] . \tag{6}$$

In Figure 4 we show the distributions of the various obtained geometrical parameters, i.e., the distribution of loop lengths $N(l)$, of the loop widths $N(w)$, of the projected loop areas $N(A)$, and of the loop volumina $N(V_{\rm EUV})$. The distribution of loop lengths extends over a range of $l \approx 3$–20 Mm and can be fitted with a power law $N(l) \propto l^{-2.10 \pm 0.11}$. The loop widths extend over a range of $l \approx 1.5$–10 Mm and can be characterized with a power law

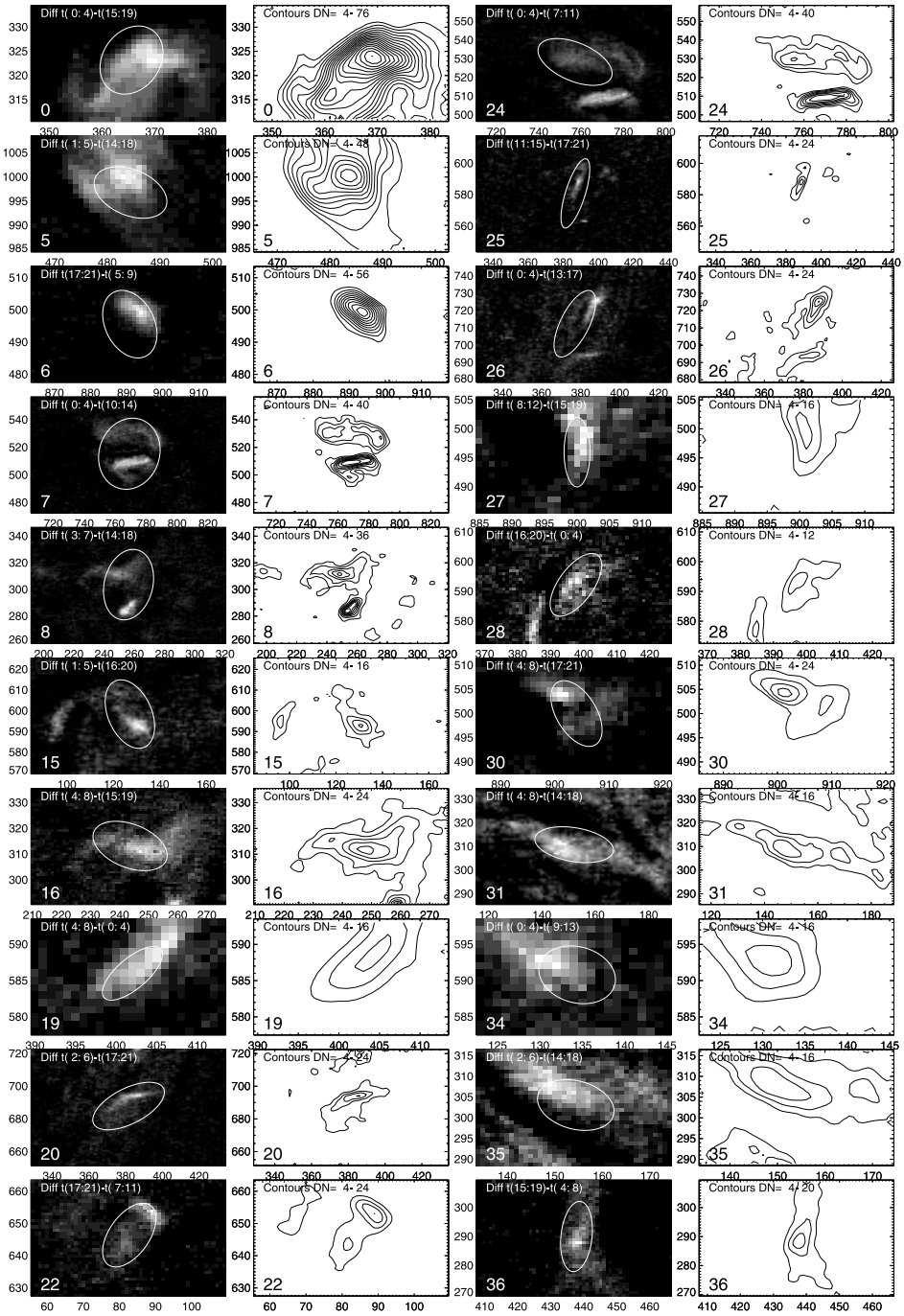

FIG. 2.—Spatial maps of 20 EUV flare events, selected from among the 36 largest events. The event numbers are sorted according to total EUV flux. The gray scales and contours were obtained from difference images taken at the peak and minimum time of each flare and averaged over five cadences. The contours of the difference images have an increment of 4 DN.

$N(w) \propto w^{-4.43 \pm 0.22}$. The loop areas cover a range of $A \approx 4$–200 Mm^2 and can be described with a power law $N(A) \propto A^{-2.56 \pm 0.08}$, while the loop volumina have values of $V_{\rm EUV} \approx 20$–5000 Mm^3 and their distribution can be characterized with a power law $N(V_{\rm EUV}) \propto V_{\rm EUV}^{-1.94 \pm 0.09}$.

2.2. *Physical Parameters*

The flux f (or photon count rate) emitted from an optically thin plasma is essentially proportional to the emission measure EM(T_e) at the peak temperature of the instrumental response function. For *TRACE*, the peak temperature of the 195 Å wavelength passband is $T_{195} \approx 1.4$ MK, while the peak temperature is $T_{171} \approx 1.0$ MK in the 171 Å wavelength passband (see description of *TRACE* response functions in the Appendix and Fig. 12). When the emission can be assumed to be isothermal, it is customary to calculate an emission measure–weighted temperature from two wavelengths with a filter-ratio method. For flare events, however, the assumption of an isothermal plasma is time-dependent because the flare plasma is subject to substantial heating and cooling, as it will be quantified in § 2.3. In order to quantify these dynamic processes we specify the

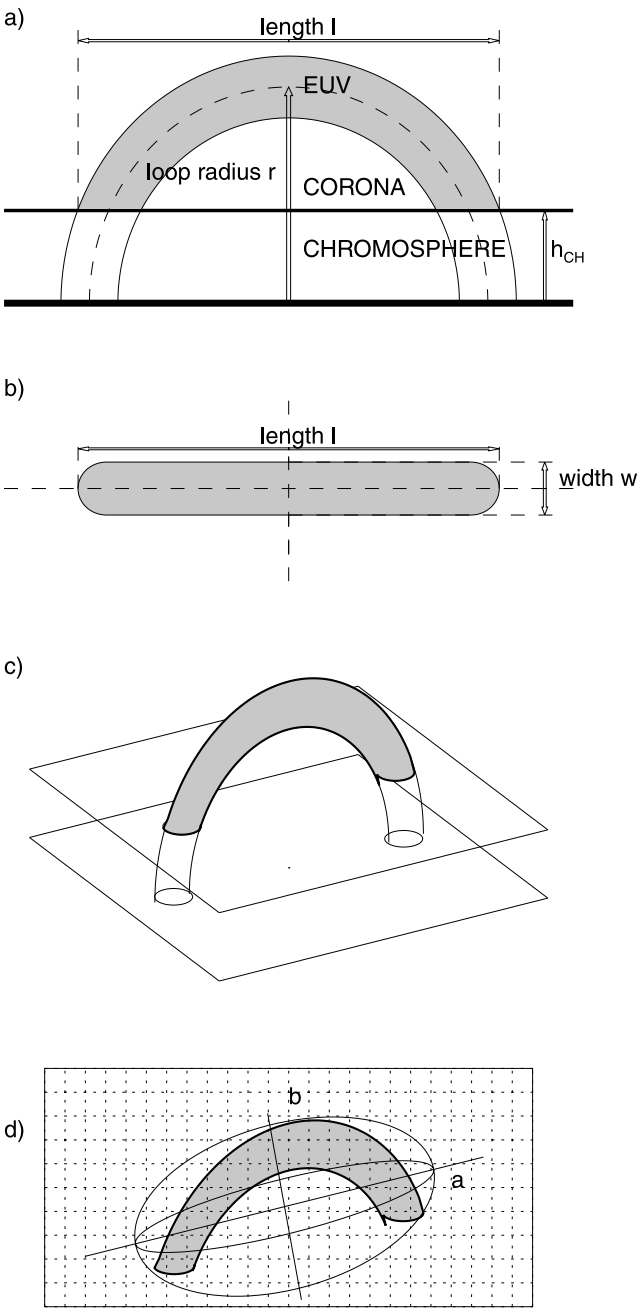

FIG. 3.—Geometric model of semicircular, cylindrical loop model used to quantify length l, width w, and radius r of EUV microflare loops. Because these flare loops are relatively small, the chromospheric segments (with a height of $h_{Ch} = 2500$ km) are truncated from the coronal, EUV-luminous loop volumes. The bottom panel illustrates how the ellipsoidal axes a and b confine the projected loop geometry, from which the projected length l and width w is determined with eqs. (2) and (3).

emission measure as function of temperature and time, $\mathrm{EM}(T_e, t)$. Using the two available wavelengths 171 and 195 Å, however, we can sample the differential emission measure distribution $d\mathrm{EM}(T_e, t)/dT_e$ at two temperatures only. Because our microflare selection is based on the 195 Å data set, we use the corresponding temperature ($T_{195} = 1.37$ MK) as primary reference for the emission measure EM_{195} distribution. The distribution of peak emission measures (evaluated at the pixels with maximum flux during each flare) is shown in Figure 4 (*bottom left*), which can be characterized by a power-law distribution $N(\mathrm{EM}) = \mathrm{EM}^{-2.92\pm0.15}$ in the range of $\mathrm{EM} = 2 \times 10^{25}$–$3 \times 10^{26}$ cm^{-5}.

From the emission measure $\mathrm{EM} = \int n_e^2(z)dz$ one can determine the electron density, if the filling factor and column depth are known. If we adopt a cylindrical flux tube model with circular loop cross section (Fig. 3 [*top*]) for our microflares, the column depth (along the line of sight) can be deduced from the transverse loop width w (measured in the plane of sky). For a homogeneous loop with constant density and filling factor of unity, the electron density n_e measured at a location with perpendicular viewing angle is then

$$n_e = \sqrt{\frac{\mathrm{EM}}{w}} \,. \tag{7}$$

The electron densities thus determined for our sample of 281 EUV microflare loops is found in a range of $n_e = (0.2\text{–}0.9) \times 10^9$ cm^{-3}. The corresponding pressure (with the Boltzmann constant $k_B = 10^{-15.86}$ ergs K^{-1} and temperature $T_e = 1.37$ MK),

$$p = 2 n_e k_B T_e \,, \tag{8}$$

is found in a range of $p = 0.07$–0.32 dyn cm^{-2}.

The total thermal energy contained in these flare loops can then be estimated by integrating over the EUV-emitting loop volume (eqs. [4]–[6]),

$$E_{th} = 3 n_e k_B T_e V_{EUV} \,, \tag{9}$$

which yields energies in the range of $E_{th} = 1 \times 10^{24}$–$2 \times 10^{26}$ ergs. The frequency distribution of thermal energies $N(E_{th})$ is shown in Figure 4 (*bottom right*), which can be fitted by a power-law distribution $N(E_{th}) \propto E_{th}^{-1.79\pm0.08}$. Note that this power-law slope is similar to that found for the total (area-integrated) EUV flux (Paper I, Fig. 12 [*bottom*]), i.e., $N(\Delta F) \propto \Delta F^{-1.85\pm0.05}$.

In Figure 5 we show correlations between some physical parameters. We do not find any correlation between the electron density or pressure with a geometric parameter. However, the total thermal energy per flare scales with the geometric size (length, area, volume) or total flux of the flare. Because the electron density n_e scales with the flare loop width, $n_e \propto w^{-1/2}$ (eq. [7]), while the temperature is essentially constant ($T_e \approx 1.4$ MK) for our data set selected at 195 Å, we expect a relation of $E_{th} \propto w^{-1/2} V_{EUV}$ according to equation (9). This is approximately satisfied by the data, which show $E_{th} \propto V_{EUV}^{1.0}$ (Fig. 5 [*bottom right*]). If the loop width w would be proportional to the loop length l, we would expect the relations $E_{th} \propto l^{5/2}$ and $E_{th} \propto A^{5/4}$. The data show similar correlations, namely $E_{th} \propto l^{2.1}$ and $E_{th} \approx A^{1.4}$. The minor difference probably occurs because the loop width is not exactly proportional to the loop length. We emphasize that the correlation $E_{th} \propto A^{3/2}$ is a consequence of our cylindrical flare loop model, which differs from other studies (e.g., Krucker & Benz 1998), in which a constant column depth was assumed and thus constrains a different scaling ($E_{th} \propto A^{1.0}$).

2.3. *Temperature Evolution*

Our novel flare criterion adopted in Paper I, based on temporal, spatial, and dynamic correlations between two temperature regimes, requires a physical justification. In

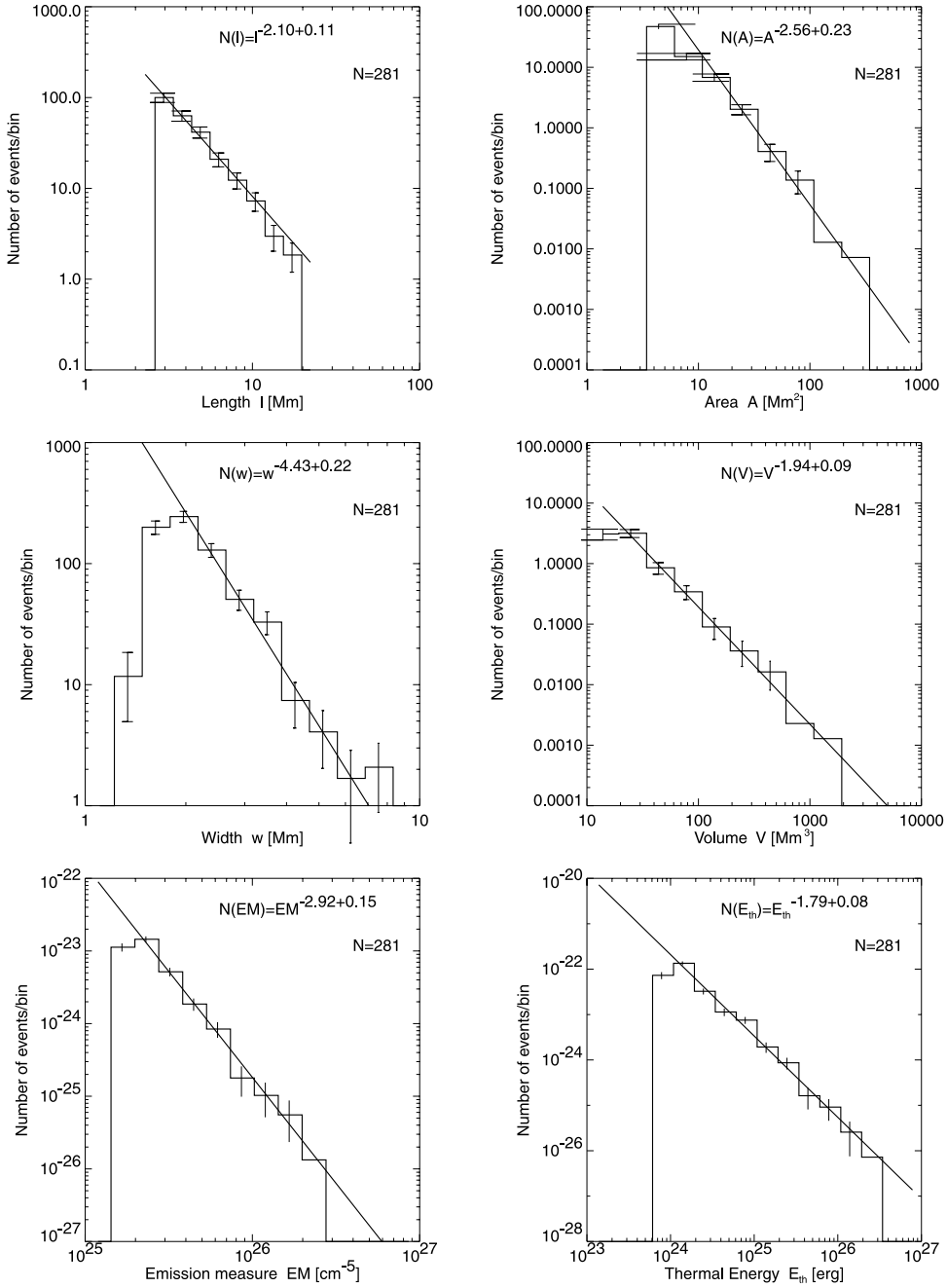

FIG. 4.—Power-law fits to distributions of six physical parameters: length l, width w, loop area A, loop volume V, emission measure EM, and thermal energy $E_{\rm th}$.

this section we investigate the correlated behavior between the time profiles of the two temperatures $T_{171} = 0.9$ MK and $T_{195} = 1.4$ MK and relate their coevolution to flare heating and cooling processes.

Figure 6 shows the time profiles $F_{171}(t)$ and $F_{195}(t)$ for the same subset of 20 flares for which spatial maps $f_{195}(x, y)$ are shown in Figure 2. This selection shows a representative subset of time profiles among the 281 detected EUV flares. The set of 20 flares shown in Figure 6 also reveals typical flare durations and occurrence rates at cospatial positions. The time interval shown in Figure 6 comprises 22 cadences (each 125 s), spanning over $\approx$45 minutes. During this interval we find that in most flare locations only one single dominant flare occurs, but we observe occasionally a secondary minor flare burst. Applying a 3 σ criterion to separate subsequent significant flux enhancements, we observe a secondary flare burst only in six of 20 cases (cases 7, 22, 25, 27, 28, and 36). The selection in Figure 6 shows various complexity in the time profiles: (1) simple flares with a rapid rise and a somewhat longer (exponential-like) decay (e.g., cases 8, 15, 16, 20, and 34), (2) flare decay phases with missing rise phase (e.g., cases 0, 5, 7, 24, 26, 31, and 35), (3) flare rise phases with missing decay phase (e.g., cases 6, 22, and 36), or (4) multiple time substructures (e.g., cases 7, 22, 25, 27, 28, and 36).

A conspicuous characteristic is that the time profiles in the two temperature bands always exhibit a very similar coevolution, as expected from the high temporal cross-

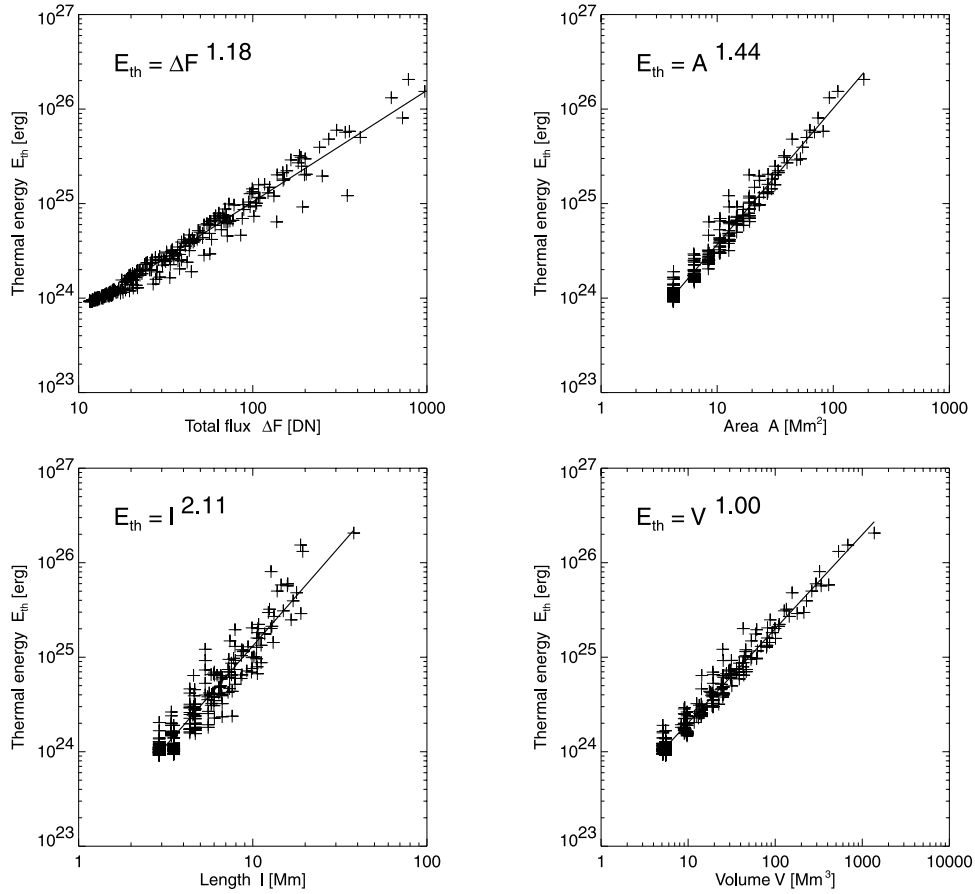

FIG. 5.—Correlations between geometric parameters (length l, area a, volume V) and thermal energy $E_{\rm th}$. The thermal energy $E_{\rm th}$ is also correlated with the total flux ΔF.

correlation coefficient $\mathrm{ccc}_t > 0.5$, as required by the flare selection criterion. Another characteristic, which is not constrained by the flare selection criterion, is a time delay of about a minute between the peaks seen of the cooler temperature ($T_{171} = 1.0$ MK) with respect to correlated peaks in the hotter temperature ($T_{195} = 1.4$ MK). This time delay can most clearly be seen in the representation of normalized time profiles shown in Figure 6. In Figure 7 we show the distribution of time delays between the two temperatures for all 281 flare events detected in 195 Å . We corrected the time offset of a half-cadence ($\Delta t_{\rm interleave} = -\Delta t/2 = 63.5$ s) of the interleaved recording mode in the relative timing between the 171 and 195 Å images. For 244 of 281 flare events we measured a cross-correlation time delay within the range of $\pm 2\,\Delta t + \Delta t_{\rm interleave} = \pm 250$ s. In 56% (136 flare events) we find a positive time delay $\tau = t_{171} - t_{195}$ of the cooler profile (F_{171}) with respect to the hotter time profile (F_{195}). The distribution of time delays can be fitted with a Gaussian, having a mean and standard deviation of $\tau = 16 \pm 70$ s (Fig. 7). The trend of a positive delay is significant, because the standard error of the mean, $m_\tau = \sigma_\tau/\sqrt{N} = 70/\sqrt{244} = 4.5$ s, is about 3 times smaller than the mean value τ.

In order to understand the observed time delay we simulate a simple flare evolution model and take the *TRACE* response functions in the two temperature bands into account. We mimic the temperature evolution during a flare simply by a rapid increase to a maximum temperature of $T_{\rm max} = 2.0$ MK and a subsequent exponential cooling phase with a time constant of $\tau_{\rm cool} = 20$ minutes (see Fig. 8 [*top panel*]),

$$T(t) = T_{\rm max} \exp\left(\frac{t - t_0}{\tau_{\rm cool}}\right), \quad \text{for } t > t_0\,. \tag{10}$$

We assign a constant density $n_e = 10^9$ cm^{-3} to the cooling flare plasma (in order to demonstrate the temperature-related effects separately), a loop width of $w = 2$ Mm, yielding a constant emission measure of $\mathrm{EM}_0 \approx n_e^2 \times w = 2 \times 10^{26}$ cm^{-5} at any temperature. Figure 12 (in the Appendix) shows the instrumental response functions $R_{171}(T)$ [and $R_{195}(T)$] of the *TRACE* 171 Å (and 195 Å) wavelength passbands, which peak at 1.0 and 1.4 MK. The fluxes recorded in the two wavelength passbands are then

$$f_{171}(t) = \mathrm{EM}(t)\Delta t R_{171}(T[t])\,, \tag{11}$$

$$f_{195}(t) = \mathrm{EM}(t)\Delta t R_{195}(T[t])\,, \tag{12}$$

where we use a constant value for the emission measure $\mathrm{EM}(t) = \mathrm{EM}_0$ here, a time step $\Delta t = 1$ s, and the time dependence of the temperature $T(t)$ is specified with equation (10). The evolution of the fluxes (Fig. 8 [*middle*]) shows the following steps. The flare plasma has an initial temperature of 2.0 MK (at $t = t_0 = 4$ minutes). When it cools down to 1.4 MK (at $t = 12$ minutes) the flux $f_{195}(t)$ peaks first, while the flux $f_{171}(t)$ peaks later on (at $t = 20$ minutes) when the plasma cooled down to 1.0 MK (Fig. 8 [*top*]). The cross-correlation between the two time profiles yields a time delay of $t_{171} - t_{195} \approx 8$ minutes. The

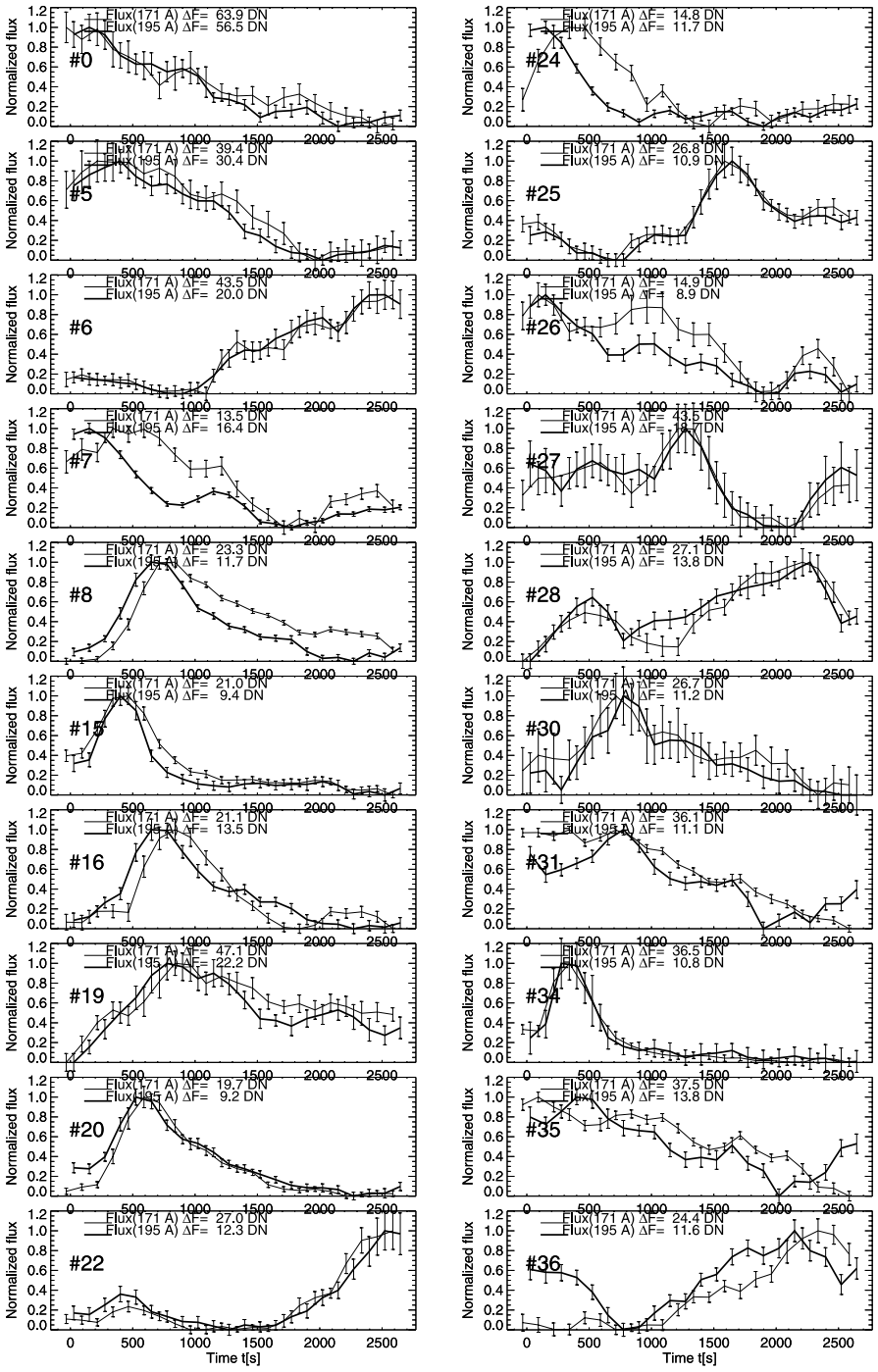

FIG. 6.—Time profiles of the 171 (*thin lines*) and 195 Å (*thick lines*) flux of the same 20 EUV microflares shown in Fig. 2. Both fluxes are normalized to unity, while the absolute fluxes are indicated in each panel. The error bars include all data noise components specified in Paper I. Note that the 171 Å flux is highly correlated with the 195 Å flux, but generally delayed.

evolution of the filter ratio $q(t) = f_{195}(t)/f_{171}(t)$ drops from an initial high value $q \gg 1$ monotonically to a very low value $q \ll 1$ during the time interval of $t = 4$–30 minutes (Fig. 8 [*bottom*]).

As an alternative to an initially hot flare, with an initial temperature that is hotter than *TRACE* passbands used here, we also simulate an initially cool flare, with an initial temperature of $T_{\max} = 1.0$ MK. Such a cool flare shows no appreciable response in the *TRACE* 195 Å passband (see dashed lines in Fig. 8), and its evolution is only seen in the *TRACE* 171 Å passband. This different behavior clearly demonstrates that we can distinguish between initially hot and cool microflares. This way we can even constrain the initial flare temperature in the range of $0.7 \lesssim T_{\max} \lesssim 1.8$ MK.

We now select a subset of flares that show a relatively simple time evolution, namely a single peak with a rapid rise and subsequent decay. In Figure 9 we show the time profiles $f_{171}(t)$ and $f_{195}(t)$ of 12 flare events with such a simple time evolution. Assuming a flare plasma with a single temperature $T_e(t)$ and density $n_e(t)$ value at a given time, we can directly invert the time evolution of the

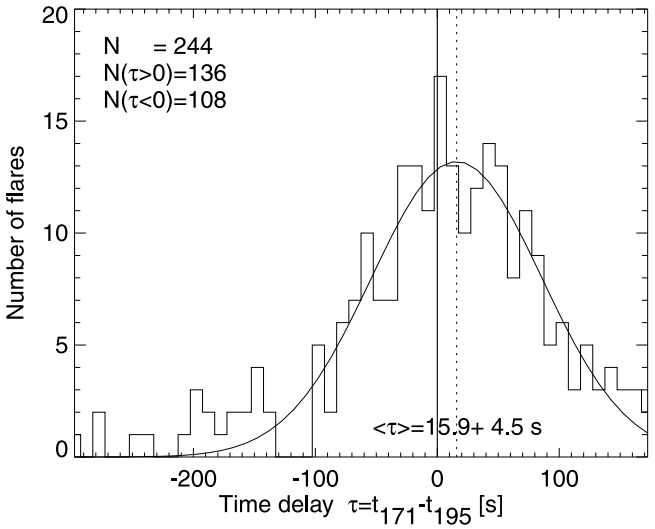

FIG. 7.—Distribution of the time delays of the 171 Å channel with respect to the 195 Å channel. The average and standard error is $\langle \tau_{\rm delay} \rangle = 15.9 \pm 4.5$ s.

electron temperature $T_e(t)$ from the flux filter ratio $q(t)$,

$$q(t) = \frac{f_{195}(t)}{f_{171}(t)} = \frac{R_{195}[T_e(t)]}{R_{171}[T_e(t)]} \,. \tag{13}$$

The inversion of the 195 Å /171 Å filter ratio yields unique temperature values in the range of $T_e = 0.7$–1.8 MK. We show the inferred temperatures of 12 flares in Figure 9. The data show that the temperature drops in all 12 selected flares, with a steepest gradient $dT_e(t)/dt$ during the flare peak time, and slower or fluctuating in the decay phase of the microflares. We can therefore clearly attribute the temperature change during the flare peak to cooling of the flare plasma. The initial flare temperature is typically found in the range of $T_{\rm max} = 1.2$–1.3 MK and drops down to $T_{\rm min} \approx 1.0$–1.2 MK. Although the filter ratio allows us to determine unique values in the range of $T_e = 0.7$–1.8 MK, the accuracy of the filter-ratio method crucially depends on the accuracy of the (flare-unrelated) background subtraction. If we estimate the background subtraction (here defined by the minimum flux value of the time series) to be accurate to 10%, we can measure filter ratios only in the range of $0.1 < q(t) < 10$, which limits the temperature inversion range to $T_e = 0.9$–1.8 MK for the *TRACE* 195/171 filter ratio. For a 20% error in the background subtraction, temperature inversion is restricted to $T_e = 0.98$–1.54 MK. Despite these restrictions, we do not find any initial flare temperature above $T_{\rm max} \approx 1.3$ MK, and we thus conclude that most of the microflares observed here (simultaneously in the 171 and 195 Å TRACE channels) do not support the view that such EUV microflares represent the late cooling phase of initially hotter SXR-bright microflares.

We consider now the observed cooling times of the 12 microflares shown in Figure 9. We fit an exponential time profile $T(t)$ with a cooling time constant $\tau_{\rm cool}$ (eq. [10]) to the steepest time segment during the flare peak phase. Other time segments with less steep temperature gradients $dT_e(t)/dT$ are likely to yield overestimates of the cooling time because they are likely to represent superpositions of subsequent heating cycles. For the 20 flares we find cooling times in the range of $\tau_{\rm cool} = 33$–352 minutes, with a median

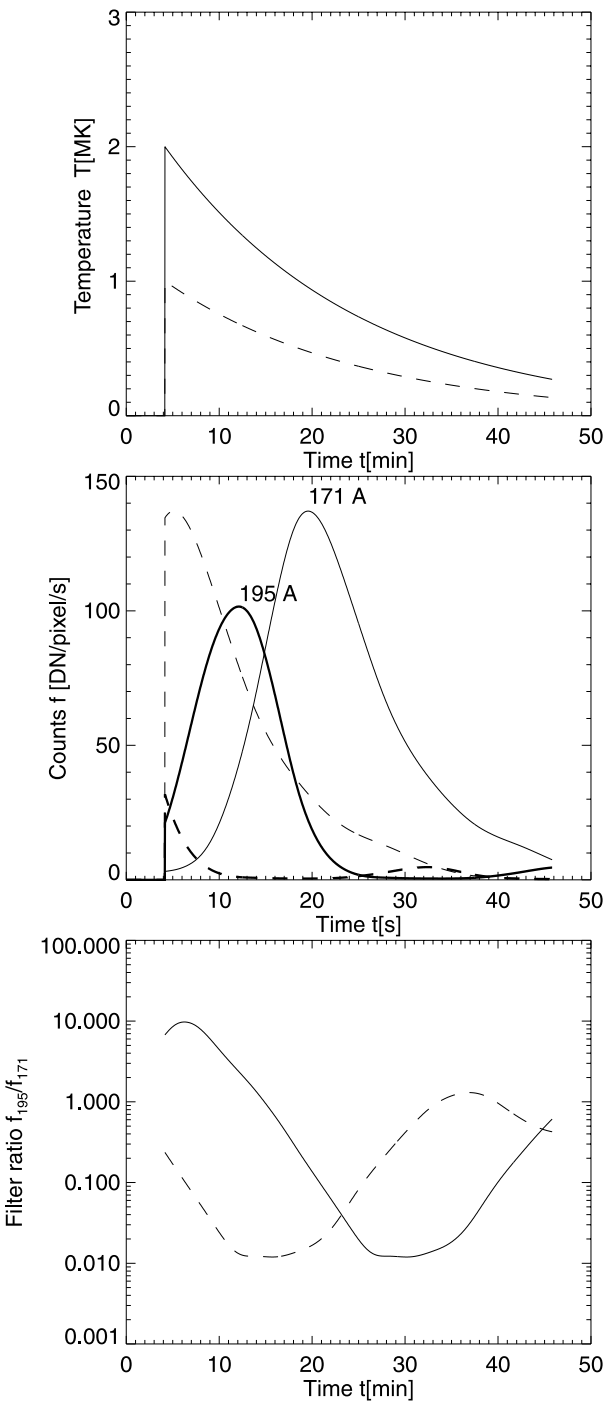

FIG. 8.—Model of a cooling flare, showing the evolution of the temperature (*top*), the 171 and 195 Å fluxes (*middle*), and the filter ratio (*bottom*). A flare with an initial hot temperature (2 MK) is shown with a solid line, and another flare with an initial cool temperature (1 MK) is shown with a dashed line. Note the relative delays of the flux peak times.

value of 78 minutes. If we place the initial temperature to the peak temperature of the 195 Å passband, i.e., $T_{\rm max} = 1.37$ MK, we would expect the EUV emission to peak in the 171 Å passband at a time interval of $t_{171} - t_{195} = 78 \ln(0.96/1.37) = 28$ minutes later. However, the actually measured cross-correlation delays are found in the range of $\tau_{\rm ccc} = 0$–4 minutes for these 12 flares. This indicates either that the initial flare temperature is below the peak

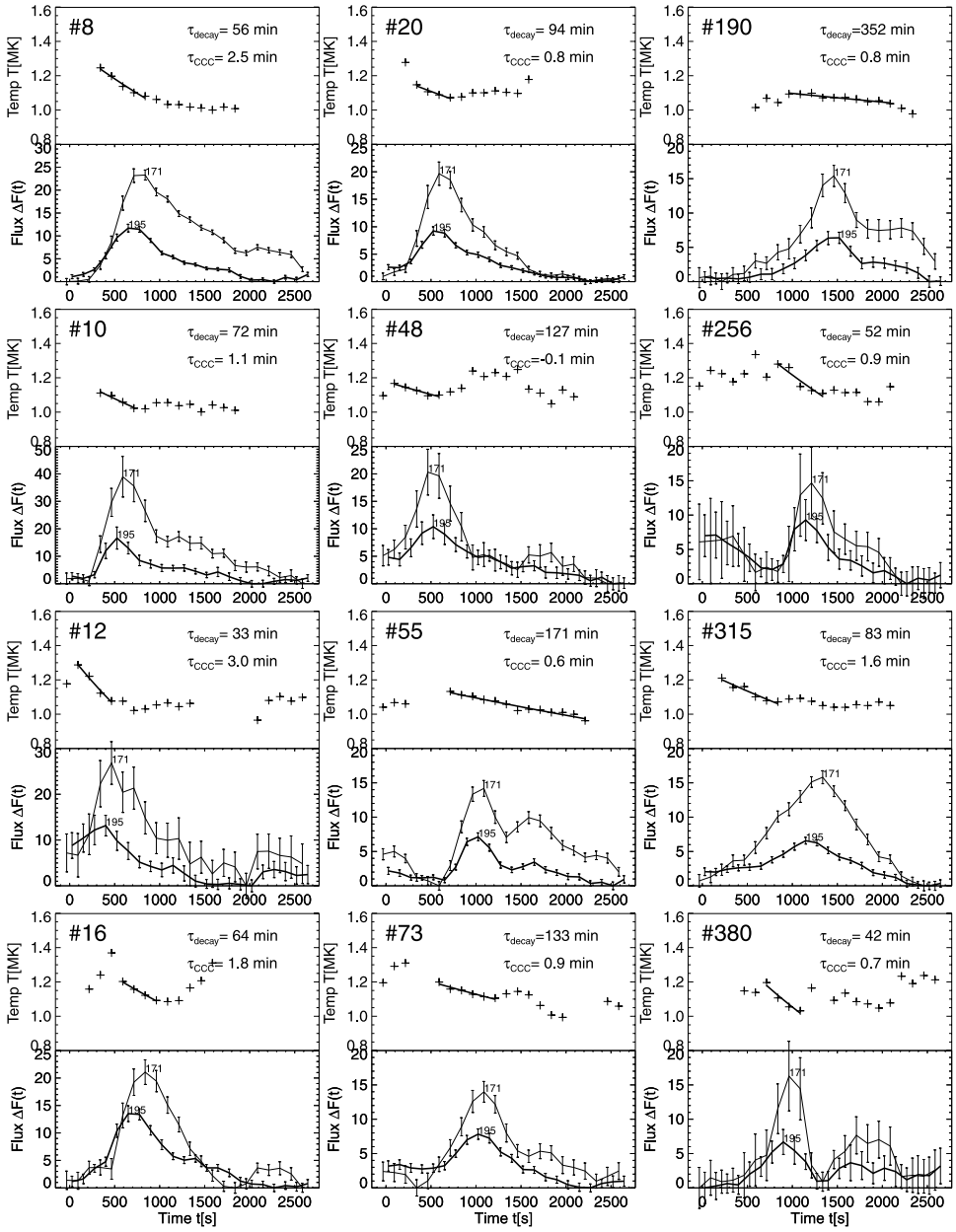

FIG. 9.—Flux and temperature evolution of 12 flares, selected by the criteria of simplicity in time structures (rise plus decay) and high signal-to-noise ratio. The temperature evolution (determined from the inversion of the filter ratio) shows in all cases a temperature decrease during the main flare peak phase, which is fitted with an exponential function (*thick line in top panels*), with the decay time constant τ_{decay} indicated. The cross-correlation delay τ_{ccc} is also given for comparison.

temperature of the 195 Å passband or that the density drops faster than the cooling time. We investigate the evolution of the electron density during EUV microflares in the next section.

2.4. *Density Evolution and Radiative Cooling*

The evolution of the electron density $n_e(t)$ can be obtained from the filter-ratio temperature $T_e(t)$ [after the inversion of $R(T_e[t])$, eq. (13)] and the flux definition $f_{195}(t)$ (eq. [12]),

$$n_e(t) = \sqrt{\frac{\mathrm{EM}(t)}{w}} = \sqrt{\frac{f_{195}(t)}{w \Delta t R_{195}(T_e[t])}} \,. \qquad (14)$$

The 12 microflares selected in Figure 9 have peak flux increases in a range of $f_{195} = 6$–12 DN, loop widths of $w = 1.8$–7.2 Mm, yielding emission measures of $\log(\mathrm{EM}\ [\mathrm{cm}^{-5}]) = 25.08$–$25.50$, and electron densities of $n_e = (0.13\text{–}0.37) \times 10^9\ \mathrm{cm}^{-3}$ (Table 1). Because the electron density $n_e(t)$ is proportional to the emission measure $\mathrm{EM}(t)$, the evolution can directly be seen from the flux profiles $f_{171}(t)$ and $f_{195}(t)$ shown in Figure 9. The flux of the 12 simple flares shown in Figure 9 decays on timescales of 4–30 minutes down to a level of $\lesssim 10\%$, during which the electron density drops by a factor of $\sqrt{10} \approx 3$. In order to understand the physical nature of the temperature and density decrease in the flare decay phase we compute the conductive and radiative cooling rates for the flare plasma in the following.

The radiative loss function $\Lambda(T)$ has been recalculated by Martens, Kankelborg, & Berger (2000) for coronal elemental abundances (Feldman 1992) and the ionization balance

TABLE 1

PHYSICAL PARAMETERS OF 12 EUV MICROFLARE EVENTS

	TEMPERATURE		FLUX									
FLARE NUMBER	Begin (T_1) (MK)	End (T_2) (MK)	171 Å (f_{171}) (DN)	195 Å (f_{195}) (DN)	EMISSION MEASURE log(EM) log(cm^{-5})	LOOP LENGTH l (Mm)	LOOP WIDTH w (Mm)	ELECTRON DENSITY $n_e/10^9$ (cm^{-3})	TIME DELAY t_{ecc} (minutes)	DECAY TIME t_{decay} (minutes)	RADIATIVE COOLING t_{rad} (minutes)	CONDUCTIVE COOLING t_{cond} (minutes)
8	1.25	1.08	23.30	11.57	25.31	19.37	6.09	0.18	2.53	56.33	72.68	7.29
10	1.11	1.02	38.97	14.81	25.50	6.02	2.24	0.37	1.12	72.80	25.27	1.91
12	1.29	1.08	26.84	12.68	25.32	5.77	2.34	0.30	3.01	33.48	49.19	0.97
16	1.20	1.09	21.08	13.45	25.30	9.90	3.53	0.24	1.76	64.87	50.43	2.70
20	1.15	1.07	19.67	9.04	25.23	15.88	5.05	0.18	0.82	94.47	56.98	6.00
48	1.17	1.10	20.33	9.80	25.25	4.35	3.08	0.24	−0.14	127.84	45.64	0.57
55	1.13	0.96	14.19	6.77	25.08	14.54	7.18	0.13	0.61	171.92	77.78	3.66
73	1.20	1.11	14.00	7.54	25.11	12.73	3.17	0.20	0.89	133.40	59.24	3.79
190.....	1.09	1.04	15.41	6.37	25.11	7.36	2.90	0.21	0.76	352.31	43.06	1.67
256.....	1.28	1.11	14.69	8.61	25.12	2.90	1.84	0.27	0.86	52.05	54.30	0.22
315.....	1.21	1.07	15.82	6.42	25.10	13.09	2.85	0.21	1.61	83.62	58.22	4.10
380.....	1.20	1.03	16.28	6.06	25.12	2.90	1.84	0.27	0.68	42.23	44.41	0.26

NOTE.—Detected 1998 February 17 with the *TRACE* telescope in the 171 and 195 Å wavelengths.

of Cook et al. (1989) in order to be consistent with the newly calculated TRACE response functions $R(T)$ (see the Appendix). The new-calculated radiative loss function $\Lambda(T)$ is shown in Figure 3 of Martens et al. (2000). In the temperature range of $T_e = 1$–5 MK, which includes the *TRACE* EUV bands, the radiative loss function can be approximated by

$$\Lambda(T) \approx 10^{-21.0}\left(\frac{T}{1\ \mathrm{MK}}\right)^{-2.0} \mathrm{ergs\ s^{-1}\ cm^3}\ , \qquad 1 < T < 5\ \mathrm{MK}\ . \quad (15)$$

Note that the value $\Lambda(T)$ is about a factor of 4 higher for coronal abundances (Feldman 1992) than for chromospheric abundances (Meyer 1985; Grevesse & Sauval 1998) and a similar factor of 4 higher (at $T = 1.4$ MK) than the widely used loss function calculated by Raymond [$\Lambda(T) = 10^{-21.94}$ at $T = 0.5$–2.0 MK; see Fig. 10 in Rosner, Tucker, & Vaiana 1978].

We calculate now the radiative cooling time for the 12 microflares selected in Figure 9,

$$\tau_{\mathrm{rad}} = \frac{E_{\mathrm{th}}}{dE_R/dt} = \frac{3 n_e k_{\mathrm{B}} T_e}{n_e^2 \Lambda(T_e)}\ , \quad (16)$$

using the observed peak electron densities n_e and initial temperatures T_1 (Table 1). We obtain radiative cooling times in the range of $\tau_{\mathrm{rad}} = 33$–129 minutes, with a median value of 68 s. Comparing these values the observed exponential decay times $\tau_{\mathrm{decay}} = 33$–352 minutes, with a median of value of 78 minutes, we find both value ranges compatible. The ratio of the observed to the theoretical cooling time has a median value of $\tau_{\mathrm{decay}}/\tau_{\mathrm{rad}} = 1.02$ and varies over a range $\tau_{\mathrm{decay}}/\tau_{\mathrm{rad}} = 0.5$–2.0 for the median 67% of the events. We can therefore conclude that the plasma cooling during the rise phase of the flare is compatible with radiative cooling. The fact that the electron densities derived from the emission measure yield a radiative cooling time that agrees with the observed cooling time implies also that the filling factor of the flare loop plasma is close to unity.

In a next step we calculate the conductive cooling times for the 12 microflares selected in Figure 9,

$$\tau_{\mathrm{cond}} = \frac{3 n_e k_{\mathrm{B}} T_e}{\nabla F_C} \approx 1.1 \times 10^{-9} n_e T_e^{-5/2} L_0^2\ , \quad (17)$$

with the loop half-length $L_0 = L/2$. We find conductive cooling times in a range of $\tau_{\mathrm{cond}} = 0.2$–7.3 minutes, with a median of 2.3 minutes. These conductive cooling times in EUV microflares here turn out to be much shorter than in larger flares. This effect probably results from a shorter loop length and a lower electron density, which is here ($n_e \lesssim 10^9$ cm^{-3}) about 2 orders of magnitude smaller than in SXR-bright larger flares ($n_e \approx 10^{11}$ cm^{-3}), leading to a 2 orders of magnitude shorter conductive cooling time. This effect leaves us with the unusual situation that the expected conductive cooling time is about a factor of 30 shorter than the calculated radiative cooling time or the observed flare decay time. The relatively slow observed cooling, which is much longer than the conductive cooling time, can be explained if the flare loops are continuously or cyclically heated, e.g., by chromospheric evaporation upflows, which smooth out the steep temperature gradients across the transition region, and in this way reduce the conductive cooling rate. Given this scenario we may interpret smoothly varying flare curves (on timescales of $\approx$30 minutes) as continuous heating processes, while rapid varying flare curves (on timescales of $\gtrsim$2 minutes) indicate intermittent heating. The 12 examples shown in Figure 9 exhibit a variety of flare episodes on timescales of $\lesssim$3–30 minutes.

3. DISCUSSION

3.1. *Comparison of EUV Nanoflares with Larger Flares*

We address first the question how the analyzed EUV microflares intercompare with physical parameters from larger flares, which are primarily studied in SXR and HXR. We compile the physical parameter ranges (electron temperature T_e, electron density n_e, and spatial scales l) of statistical flare data sets from different wavelengths in Table 2, and compute the resulting ranges of the following parameters: pressure p (eq. [8]), emission measure EM (eq. [7]), thermal energy E_{th} (eq. [9]), radiative cooling time τ_{rad} (eq. [16]), conductive cooling time τ_{cond} (eq. [17]), and the effective cooling time τ_{cool}, which is defined to be the shorter of the two. We divide the physical parameters into three groups, depending on whether they have been analyzed in EUV, SXR, or HXR. The physical parameters were obtained from statistical flare studies in EUV (Berghmans et al. 1998; Krucker & Benz 1998; Parnell & Jupp 2000; and this study), in SXR (Shimizu et al. 1992; Culhane et al. 1994; Feldman et al. 1996; Shimizu 1997; Sterling et al. 1997; Nitta & Yaji 1997; Aschwanden & Benz 1997), and HXR (Crosby et al. 1993; McTiernan, Fisher, & Li 1999) The temperature ranges of these three groups are approximately 1–2 MK (EUV flares), 2–10 MK (SXR flares), and 5–50 MK (HXR flares). Interestingly, the flares detected in these three different wavelength and temperature regimes (EUV, SXR, HXR) constitute also three almost non-

TABLE 2

PHYSICAL PARAMETERS AS FUNCTION OF FLARE SIZE

Parameter	Nanoflares	Microflares	Flares
Wavelength regime	EUV	SXR, EUV	EUV, SXR, HXR
Temperature T_e (MK)	1–2	2–10	5–50
Spatial scale l (Mm)	2–20	5–50	10–100
Electron density n_e (cm^{-3})	2×10^8–10^9	10^9–10^{10}	10^{10}–10^{12}
Electron pressure p (dyn cm^{-2})	0.1–0.4	1–15	30–6000
Emission measure EM (cm^{-5})	10^{25}–5×10^{26}	5×10^{26}–10^{29}	10^{29}–2×10^{33}
Thermal energy E_{th} (ergs)	5×10^{23}–5×10^{26}	10^{26}–2×10^{29}	10^{29}–4×10^{32}
Radiative cooling times τ_{rad} (minutes)	10 minutes–3 hr	12 minutes – 2 days	4 minutes – 10 days
Conductive cooling times τ_{cond} (minutes)	2 s–5 minutes	2 s–20 minutes	3 s–6 hr
Cooling time τ_{cool} (minutes)	2 s–3 minutes	2 s– 8 minutes	3 s–20 minutes

overlapping energy ranges, which naturally may be dubbed the regimes of *nanoflares* (10^{24}–10^{27} ergs), *microflares* (10^{27}–10^{30} ergs), and (*milli*)*flares* (10^{30}–10^{33} ergs), because their lower bounds represent fractions of 10^{-9}, 10^{-6}, and 10^{-3} of the largest flare energies at $E_{\rm th} \approx 10^{33}$ ergs. Also, the parameter ranges of electron densities, pressure, and emission measure are nonoverlapping for these three flare size groups. From the parameter ranges compiled in Table 2 we can derive the following approximate statistical scaling trends among the three (EUV, SXR, HXR) wavelength groups (see also Aschwanden 2000):

$$l(T) \propto T^1 , \tag{18}$$

$$n_e(T) \propto T^2 , \tag{19}$$

$$p(T) \propto T^3 , \tag{20}$$

$$\mathrm{EM}(T) \propto T^5 , \tag{21}$$

$$E_{\rm th}(T) \propto T^6 . \tag{22}$$

Some of these scaling laws are redundant, namely, the pressure $p \propto n_e \times T \propto T^2 \times T = T^3$, or the emission measure $\mathrm{EM} \propto n_e^2 \times l \propto (T^2)^2 \times T = T^5$. The latter scaling law $\mathrm{EM} \propto T^5$ agrees also roughly with a correlation plot of a larger set of *GOES* A2–X2 class flares shown by Feldman et al. (1996; their Fig. 9), where for a temperature range of $T_e = 10$–25 MK the *GOES* emission measure increases systematically by a factor of 100, as expected from $\mathrm{EM}_2/\mathrm{EM}_1 = (T_2/T_1)^5 = 2.5^5 \approx 100$. While most of the geometric and physical parameters exhibit a big-flare syndrome (i.e., they scale with a positive exponent with the flare size), we find that the timescales do not scale with the flare size. If we define the cooling time by the shorter of the conductive or radiative cooling timescale, we find that the expected range of cooling timescales varies less than an order of magnitude between the smallest nanoflare and the largest flare, while the thermal energy varies over 9 orders of magnitude. The small variation in cooling times comes mainly from the fact that the scaling of different physical parameters partially cancel each other in the expressions of the radiative and conductive cooling times. These scaling laws represent a useful tool to interpolate or extrapolate physical parameters in unobserved energy regimes. At this point we like to emphasize that the observed EUV events exhibit physical parameters (density, temperature, scales, energy) that are consistent with the extrapolation of scaling laws from larger flares observed in SXR and HXR into the micro- and nanoflare energy regime. This is another indication (besides the flare criterion based on cross-correlation coefficients; see Paper I) that the analyzed EUV events have flarelike characteristics.

3.2. *The Frequency Distribution of Microflare Energies*

The frequency distribution of flare energies, $N(E)$, is a crucial diagnostic to calculate the overall energy residing in flares contained in a given or expected energy range. We show this frequency distribution of thermal energies $N(E_{\rm th})$ of flares detected in 195 Å *TRACE* data in the context of other compatible frequency distributions in Figure 10. The energies of our EUV flare set extends from 1×10^{24} to 2×10^{26} ergs and can be fitted with a power law of $N(E_{\rm th}) \propto E_{\rm th}^{-1.79 \pm 0.08}$ (§ 2.2 and Fig. 4). The distributions shown in Figure 10 are normalized in units of 10^{-50} flare events per time unit (s^{-1}), per area unit on the solar surface (cm^{-3}), and per energy unit (ergs^{-1}). In the same energy range, another *TRACE* data set of 171/195 Å filter ratios has been analyzed by Parnell & Jupp (2000), who employ a similar variability detection algorithm (however, without discrimination of flarelike and nonflare events), and find from a number of 4497 events with a significance of $\geq 3\,\sigma$ a power-law distribution $N(E_{\rm th}) \propto E_{\rm th}^{-2.42}$. These authors fit a skew-Laplace distribution to the data to correct for potential undersampling of small events. In a slightly higher energy range, i.e., $E_{\rm th} = 0.8 \times 10^{25}$–$1.6 \times 10^{26}$ ergs, Krucker & Benz (1998) measured the first frequency distribution of EUV flares previously, using *SOHO*/EIT 171/195 Å filter ratios. In their pioneering work they found for the first time a frequency distribution with a power-law slope in excess of 2, within a range of 2.3–2.6, depending on the used threshold in significance or flare size area. In Figure 10 we show all three EUV frequency distributions on the same absolute scale, carefully normalized by the field of view and total duration of each independent observation. Some offset in the absolute value could indicate various levels of solar activity because the flare rate in HXR is known to vary by a factor of 20 between the maximum and minimum of the solar cycle (Crosby et al. 1993). The comparison in Figure 10 shows that the occurrence rates of the three measurements do not coincide at any energy, and diverge by about two orders of magnitude in their absolute values among the three studies. Unless the Sun exhibited a quite different scaling behavior during the three observations, these discrepancies are indicative of systematic methodical biases. An obvious cause for different absolute numbers is the threshold for event detection. However, various thresholds should mainly affect the weakest events at the low end of the frequency distribution, while it should have lesser effect on the strongest events. However, comparing the distributions at the upper end (say at an energy of 10^{26} ergs), Parnell & Jupp (2000) detect a factor of ≈ 10 times fewer events, while Krucker & Benz detect a factor of ≈ 10 more events than our present study. Because the total number of detected events in each study shows different relative numbers, we suspect that this discrepancy largely results from different assumptions in the calculation of the thermal energy. Investigating methodical differences that could introduce a bias in determining the power-law slope of the frequency distribution, we find three major effects: (1) The coincidence criterion for simultaneous temporal peaks in adjacent spatial pixels when combining variable pixels to flare events, i.e., $\pm \Delta t = \pm 2$ minutes here, opposed to $\pm \Delta t = 0$ in the other studies. A stricter coincidence criterion breaks a multiple-loop flare into more smaller events and thus steepens the frequency distribution. (2) The flare criterion to discriminate flare events from other nonflaring variabilities (e.g., moving plasma loops in emission or absorption, loop oscillations, photospheric footpoint motion, etc.) finds more nonflaring phenomena at weaker flux levels and thus also steepens the frequency distribution. To test this effect we disabled the flare-selection criterion and found a power-law slope that was by $\Delta\alpha = +0.3$ steeper (Paper I). (3) The assumption of a constant column depth h (in two-dimensional models) in the conversion of EUV fluxes into thermal energies forces a scaling of $E_{\rm th} \propto A$ (flare area), opposed to the flare loop cylinder (three-dimensional) model, where the column depth is equal to the transverse loop diameter, and this way implies a volume-proportional scaling $E_{\rm th} \propto V \propto A^{3/2}$. We tested the

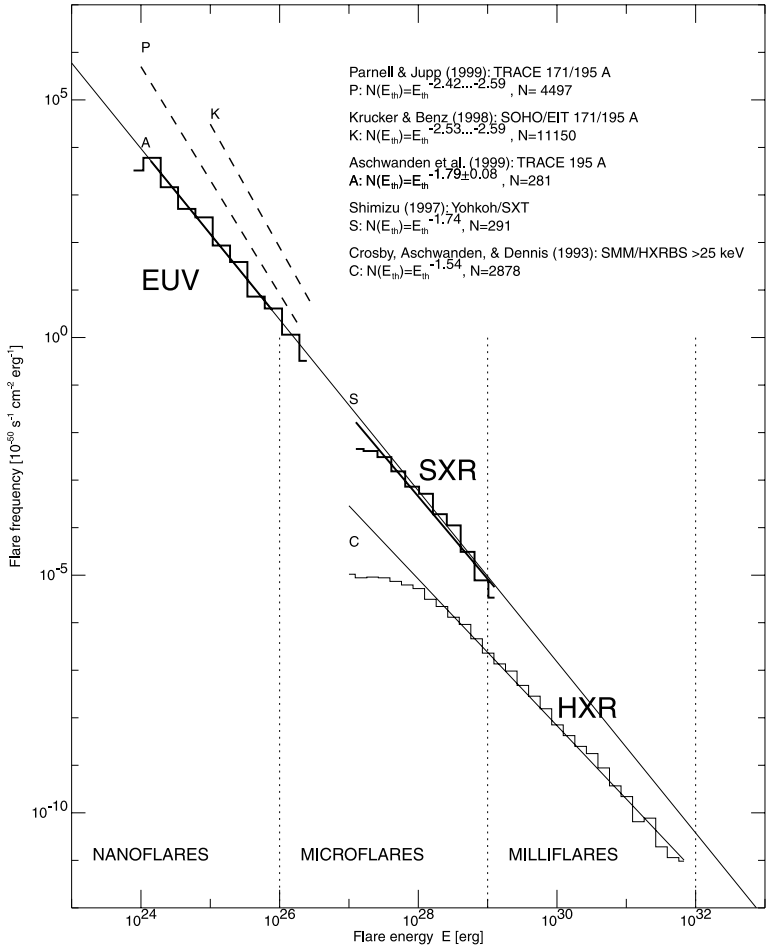

FIG. 10.—Composite flare frequency distribution in a normalized scale in units of 10^{-50} flares per time unit (s^{-1}), area unit (cm^{-2}), and energy unit ($ergs^{-1}$). The diagram includes EUV flares analyzed here (A), from Krucker & Benz (1998), from Parnell & Jupp (2000; with the steeper slope of -2.4 referring to a constant column depth, while the flatter slope of -2.0 refers to the same flare loop model as used here), the distribution of transient brightenings in SXR (Shimizu 1997) and HXR (Crosby et al. 1993). All distributions are specified in terms of thermal energy $E_{\rm th} = 3n_e k_{\rm B} T_e V$, except for the case of HXR flares, which is specified in terms of nonthermal energies in greater than 25 keV electrons. The slope of -1.8 is extended over the entire energy domain of 10^{24}–10^{32} ergs, yielding also a thermal energy estimate for the HXR flares.

effect of this assumption on the slope of the frequency distribution and found that the assumption of a constant column depth steepens the slope by $\Delta\alpha \approx +0.15$. (This effect was confirmed by Parnell & Jupp 2000, who find a slope increase by $\Delta\alpha \approx 0.4$ as a consequence of this assumption.) All three effects pull in the same direction. The three effects together steepen the power-law slope by $\Delta\alpha > +0.45$ and fully explain the methodical differences between our study (with a slope of 1.8) and the two previous EUV studies (with a slope of 2.3–2.6). While the differences among the three studies can be understood this way, the next question is the justification of the choice of methods. Obviously, the methodical choices crucially depend on a sensible flare definition that can be applied numerically. Our approach to use cross-correlation coefficients to probe temperature-correlated changes constitutes a specific restriction, namely, that heating and cooling processes are required for a flare process, while isothermal motions are automatically excluded with this criterion. Further in-depth studies are required to establish a refined flare criterion that is not subject to any energy-dependent bias.

Let us also compare the frequency distribution of EUV nano/microflares with the larger SXR and HXR flares. In Figure 10 we plot a frequency distribution of SXR transient brightenings measured in a particular active region (Shimizu 1997). The SXR parameters are given in Table 2. The absolute normalization of the occurrence rate of SXR transient brightenings shown in Figure 10 is somewhat uncertain because it is not known how many of these very active regions with frequent brightenings (as selected by Shimizu) are present on the solar disk in the average. The scaling in Figure 10 corresponds to a lower limit, in which the analyzed region is the only active one. Nevertheless, in spite of this uncertainty, the combined occurrence rates of SXR microflares and EUV nanoflares are compatible with a power-law slope of ≈ -1.8 (Fig. 10 [*thin line*]).

For larger flares, unfortunately no extensive statistics on the thermal energy content of (spatially resolved) flare loops is available. Instead, extensive statistics of nonthermal energies in greater than 25 keV HXR of flares is available, e.g., 2878 flares observed with *SMM*/HXR BS, which yield a power-law distribution of $N(E_{\rm nth}) \propto E_{\rm nth}^{-1.54}$ (Crosby et al. 1993). We do not expect that the thermal and nonthermal energies have a one-to-one correspondence. If we rescale the nonthermal energies to match the extrapolated occurrence rate of EUV and SXR microflares in Figure 10, we find that small flares (at 10^{29} ergs) have a nonthermal energy content of $\approx 10\%$, while the largest flares have a nonthermal energy

content of $\approx 30\%$. These numbers seem to be reasonable, given the fact that the spectral nonthermal tail has always a power-law slope steeper than 2 and thus contains more energy in thermal electrons than in nonthermal electrons. Moreover, since larger flares have a harder spectrum, the relative fraction of nonthermal energy is expected to increase with higher thermal energies, as observed here (from 10% to 30%). Although the exact ratio of thermal and nonthermal energies is not exactly known, the combined frequency distribution of EUV, SXR, and HXR flares seem to form a consistent distribution with an overall power-law slope of -1.8 over a range of *8 orders of magnitude in energy*, i.e., from 10^{24} to 10^{32} ergs.

3.3. *Are There Picoflares?*

Since the appearance of Parker's (1988) nanoflare concept to heat the solar corona, the search for the smallest flare signatures has been greatly stimulated, especially encouraged with the advent of new high-resolution imaging instruments. Let us discuss the physical nature of the smallest flare events we expect to observe, based on the statistics and scaling laws we obtained so far. The occurrence rate of flares as function of the energy ranges of HXR, SXR, and EUV flares is visualized in Figure 10. Because the occurrence rate of flares is now quantified down to energies of $\approx 10^{24}$ ergs, an excess in the occurrence rate at even smaller energies is needed to fulfill the heating requirement of the solar corona, estimated to be at energies of $\lesssim 3 \times 10^{23}$ ergs (Krucker & Benz 1998) or $\approx 10^{17}$–10^{24} ergs (Parnell & Jupp 2000), according to extrapolations of the power-law slope measured in the energy range of $E_{\rm th} \approx 10^{24}$–$10^{26}$ ergs. Let us call these required events *picoflares*, i.e., with energies of 10^{21}–10^{24}. An educated guess of the physical parameters of these picoflares is to extrapolate the scaling laws we know from the higher energy range (eqs. [18]–[22]). According to these scaling laws equations (18)–(22) we expect for 10^3 times smaller energies a temperature that is smaller by $T^{-3/5} = 0.25$. Since the EUV-observed nanoflares reside in the $T_e = 1$–2 MK regime, the expected temperature range of picoflares would be in the regime of $T_e = 0.25$–0.5 MK, perhaps observable in Ne V–VII, Mg VI, or Fe VIII lines. While dynamic phenomena at low temperatures have been detected in the transition region, called explosive events or microflares (e.g., Dere et al. 1989, 1991; Moses et al. 1994; Porter et al. 1995), their expected intrinsic temperature ($T_e = 0.25$–0.5 MK) is far below coronal temperatures and thus have no positive effect on heating the solar corona. To the contrary, if cool plasmas of such explosive events rise upward into the hotter corona, they would *cool the corona* and thus cannot solve the coronal heating problem at all. In other words, the bottom energy of $E_{\rm th} \approx 10^{24}$ ergs represents for flarelike events a borderline between coronal heating and cooling. The spatial scales of picoflares would be expected a factor of 4 smaller, in the range of $l = 500$–5000 km (1″–7″). This spatial scale is compatible with the height of the chromosphere ($h_{\rm Ch} \approx 2500$). If the loop is immersed in the chromosphere, EUV emission, even if produced in a chromospheric flare loop, could probably not be observed owing to the strong absorption from the ambient chromospheric plasma, so that the detection of small EUV flare loops is not possible. The electron densities would be expected a factor of 16 smaller according to the scaling law of equation (19), i.e., $n_e = (1$–$6) \times 10^7$ cm^{-3}. Because the lowest densities at the bottom of the corona range around $n_e \approx 10^8$ cm^{-3}, and all densities in the transition region and chromosphere are higher, such low densities of order 10^7 cm^{-3} cannot be balanced by the ambient plasma pressure. Based on these simple scaling arguments we do not see a viable alternative to extend the distribution of microflares and nanoflares into the regime of picoflares without violating the empirical temperature (eq. [21]), density (eq. [19]), and spatial (eq. [18]) scaling laws of flares. One could argue that different scaling laws exist for picoflares, but then the same ad hoc argument could be used against a scale-invariant power-law slope extrapolation of the occurrence rate to lower flare energies.

3.4. *Olbers's Paradox Applied to Nanoflares*

Olbers's paradox states that the number of stars per stereo angle increases quadratically with distance, which offsets the quadratic decrease of apparent brightness with distance, and thus the black sky should be bright from the summed stellar light, supposing that space is homogeneous, infinite, stationary (no big bang), and free of interstellar absorption. We have an analogous paradox for nanoflares and picoflares, if their energy increases with the area $E_{\rm th} \propto A$ and the frequency distribution has a power-law slope steeper than 2. If the number of nanoflares grows with a higher power than 2 with smaller energy, while the area occupied per nanoflare decreases only with a power of 2, there exists a critical energy $E_{\rm crit}$ at which the nanoflares fill the solar surface with a filling factor of unity, which restricts the number of smallest flares. This spatial limitation also prevents the energy integral to diverge at smaller energies $E < E_{\rm crit}$, and thus we do not have an arbitrary large energy reservoir in nano- and picoflares to heat the corona. We can estimate this critical energy $E_{\rm crit}$ where 100% of the area is covered by nanoflares from the relation

$$\frac{q_A}{1} = \frac{\int_{E_1}^{E_2} N(E)A(E)dE}{\int_{E_{\rm crit}}^{E_2} N(E)A(E)dE} = \frac{E_2^{2-a} - E_1^{2-a}}{E_2^{2-a} - E_{\rm crit}^{2-a}}, \qquad (23)$$

where q_A is the fraction of the area that is covered by integrating all nanoflare areas $A(E)$ with a frequency distribution $N(E) \propto E^{-a}$ in the energy range from E_1 to E_2. If a constant column depth is assumed in the estimate of thermal energies, the energy scales linearly with the flare area, and thus $A(E) \propto E^1$. Using the parameters from the study of Krucker & Benz (1998), $E_1 = 0.8 \times 10^{25}$ ergs, $E_2 = 1.6 \times 10^{26}$ ergs, $a = 2.6$, $q_A = 0.05$ (based on the probability of $q_{\rm pix} = 0.005$ for 3 σ enhancements per image cadence of $t_{\rm cadence} = 128$ s [see Fig. 4 in Benz & Krucker 1998] normalized with an average flare duration of $t_{\rm flare} \approx 20$ minutes, i.e., $q_A = q_{\rm pix} \times (t_{\rm flare}/t_{\rm cadence}) = 0.005 \times (1200/128) = 0.05)$], we find a critical energy of $E_{\rm crit} = 8 \times 10^{22}$ ergs. Using the parameters from the study of Parnell & Jupp (2000), $E_1 = 1 \times 10^{24}$ ergs, $E_2 = 2 \times 10^{26}$ ergs, $a = 2.42$, $q_A = 0.06$, we find a critical energy of $E_{\rm crit} = 1.6 \times 10^{21}$ ergs. If the heating of the corona requires a continuation of the power-law distribution with a slope $a > 2$ down to a zero-balance level of $E_{\rm zero}$, this requirement can be satisfied only if the area coverage limit occurs at a lower energy, i.e., $E_{\rm crit} < E_{\rm zero}$. In the case of Krucker & Benz (1998), the zero-balance level is estimated to $E_{\rm zero} = 3 \times 10^{23}$ ergs, just slightly above the area coverage limit $E_{\rm crit}$. In the case of Parnell & Jupp (2000), the zero-balance level is estimated to $E_{\rm zero} = 3.2 \times 10^{21}$ ergs, which is just a factor of 2 above the critical area coverage limit $E_{\rm crit}$.

More generally, if a frequency distribution has a power-law slope of a, $N(E) \propto E^{-a}$, and the microflare area scales with energy according to a power law $A(E) \propto E^b$, the critical condition for a 100% area coverage limit at the low end of the frequency distribution is

$$1 + b - a < 0 \, . \tag{24}$$

If the assumption of a constant column depth is made ($b = 1$), then the area limit occurs for all power-law slopes $a > 2$, as in the case of Krucker & Benz (1998) and Parnell & Jupp (2000). If a different scaling is employed, e.g., the cylindrical flare loop model used here, which leads to $E \propto V \propto A^{3/2}$ and thus $b = \frac{2}{3}$, an area limit for small flares would occur for every slope $a > 1.67$, which is the case in this study, since we found $a = 1.8$. However, because the total energy of all microflares does not diverge at small energies for slopes $a < 2$ (Hudson 1991), this additional limit is irrelevant for such cases.

3.5. *Energy Balance of Nanoflares*

An interesting self-consistency test of physical parameters in flare events can be conducted by comparing the balance between energy input and output. The average heating rate can be estimated by dividing the maximum thermal energy by the flare duration,

$$\frac{dE_{\rm heat}}{dt} \approx \frac{E_{\rm th}}{t_{\rm flare}} = \frac{3 n_e k_{\rm B} T_e V_{\rm EUV}}{t_{\rm flare}} \; ; \tag{25}$$

see definitions of $E_{\rm th}$ (eq. [9]) and flare volume $V_{\rm EUV}$ (eqs. [4]–[6]). This average heating rate amounts to $dE_H/dt = 6 \times 10^{20} \ldots 2 \times 10^{23}$ ergs s^{-1} for our set of 281 EUV nanoflares. On the other hand, this energy input has to balance the radiative and conductive loss rate. The radiative loss rate per time is

$$\frac{dE_{\rm rad}}{dt} = -n_e^2 \, \Lambda(T_e) V_{\rm EUV} \tag{26}$$

with the radiative loss function specified in equation (15). For our set of 281 nanoflares we find a radiative loss rate in the range of $dE_{\rm rad}/dt = -(3 \times 10^{20} \ldots 1 \times 10^{23})$ ergs s^{-1}. A scatterplot of the radiative loss rate versus the average heating rate is shown in Figure 11. There exists a clear correlation between the heating rate and radiative loss rate, where the radiative loss rate is on average a factor of 2 lower than the heating rate. If we assume that the conductive loss rate is of equal magnitude as the radiative loss rate (which would be expected for steady state equilibria; e.g., Vesecky, Antiochos, & Underwood 1979), the mean heating rate would balance the total losses, i.e.,

$$\frac{dE_{\rm heat}}{dt} + \frac{dE_{\rm rad}}{dt} + \frac{dE_{\rm cond}}{dt} = 0 \, . \tag{27}$$

Although steady state equibilibria are not expected in flares, we note that radiative and conductive losses have to have a similar magnitude in order to satisfy the energy budget.

3.6. *The Global Energy Flux of EUV Nanoflares*

In the previous section we discussed the energy balance between heating and radiative and conductive losses inside nanoflare loops. For the overall energy budget of the solar corona, it is more important to renormalize the heating input rate (manifested in EUV nanoflares) not selectively to the areas of flare loops but rather to average over the surface of the coronal volume over which the EUV nanoflares are sprinkled. In Paper I we measured the total area covered by EUV brightenings to 15% of the field of view in 195 Å (and 49% in 171 Å). Restricting to flarelike events, we found that only 31.1% of the 195 Å events fulfill the flare criterion (or 25.5% in 171 Å), we estimate that only a fraction of $0.3 \times 15\% = 4.5\%$ of the solar surface is covered by EUV flares. This fraction is similar to the value of 6% found by Parnell & Jupp (2000) in similar TRACE 171/195 Å data. In order to estimate the global energy flux of EUV nanoflares, i.e., the average heat energy input per area and time unit (over the surface of the observed field of view), we can simply integrate the thermal energies $E_{\rm th}$ of all microflares and divide it by the accumulated observing duration and field-of-view area,

$$P^{\rm flares} = \left\langle \frac{d^2 E_{\rm heat}}{dt \, dA} \right\rangle = \frac{\sum_{i=0}^{n_{\rm flares}} E_{\rm th}^i}{\Delta t_{\rm obs} \Delta A_{\rm FOV}} \, . \tag{28}$$

For our set of 281 EUV nanoflares we find a total accumulated thermal energy of $\sum E_{\rm th} = 2.0 \times 10^{27}$ ergs, which divided by the valid field-of-view area $\Delta A_{\rm FOV} = 8.1 \times 10^{20}$ cm^2 and the total observation duration $\Delta t_{\rm obs} = 2750$ s yields a an average energy flux of $P = 10^3$ ergs s^{-1} cm^{-2}. If we ignore the flare selection criterion, the total thermal energy flux of all EUV brightenings would only double. This energy input is about a factor of 300 below the requirement to compensate all coronal energy losses in the corona (conductive flux, radiative flux, solar wind flux), which are estimated to be $\approx 3 \times 10^5$ ergs s^{-1} cm^{-2} for the quiet Sun (Withbroe & Noyes 1977).

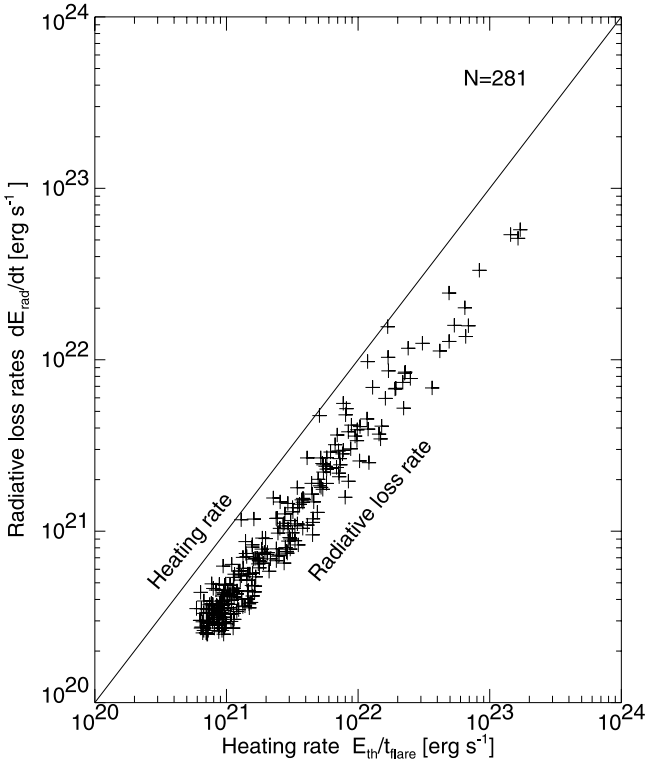

FIG. 11.—Radiative loss rate as function of the heating input rate, calculated for 281 EUV microflares. Note that the radiative loss rate does not exceed the heating rate, typically amounting to ≈50% of the mean heating rate.

3.7. *Flare Energy Budget and Coronal Heating Requirement*

While EUV nanoflares represent only a limited temperature window of the entire flare distribution, we may include also other temperature ranges (e.g., as observed in SXR and HXR) to obtain a global energy budget of flares. From the composite EUV + SXR + HXR frequency distribution of flare energies over the energy range of $E = 10^{24}$–10^{32} ergs shown in Figure 10, we established a power-law distribution with a scaling of

$$N(E) \approx 10^{-46}\left(\frac{E}{10^{24}\ \mathrm{ergs}}\right)^{-1.8}\ (\mathrm{s}^{-1}\ \mathrm{cm}^{-2}\ \mathrm{ergs}^{-1})\ ,$$

$$10^{24} < E < 10^{32}\ \mathrm{ergs}\ . \quad (29)$$

If we integrate over the entire flare frequency distribution $N(E) = N_0 E^{-a}$ with $a < 2$ and an upper energy cutoff $E_{\max}$, we obtain a total energy

$$P^{\mathrm{flares}}(E < E_{\max}) = \int_{E_1}^{E_2} N(E) E dE = \frac{N_0}{(2-a)} E_2^{2-a}\ . \quad (30)$$

For a power-law slope of $a = 1.8$ the energy content is

$$P^{\mathrm{flares}}(a = 1.8;\ E < E_{\max}) = 0.008 \times E_{\max}^{0.2}\ (\mathrm{ergs\ s}^{-1}\ \mathrm{cm}^{-2})\ . \quad (31)$$

This way we find a total (area-averaged) energy flux of $P^{\mathrm{EUV}}(E < 10^{26}\ \mathrm{ergs}) = 1.3 \times 10^3$ erg s^{-1} cm^{-2} in EUV nanoflares, $P^{\mathrm{SXR}}(E < 10^{29}\ \mathrm{ergs}) = 5 \times 10^3$ erg s^{-1} cm^{-2} in SXR microflares, and $P^{\mathrm{HXR}}(E < 10^{32}\ \mathrm{ergs}) = 2 \times 10^4$ ergs s^{-1} cm^{-2} in all flares, still an order of magnitude below the coronal heating requirement. In this energy estimates we neglected the kinetic energy, which can be as much as 2 orders of magnitude above the thermal energy (e.g., see energy estimates of the 1973 September 5 flare described in chapters by Canfield and Webb in Sturrock 1980).

4. CONCLUSIONS

In this study we analyzed geometric and physical parameters of 281 EUV nanoflares detected with the *TRACE* telescope simultaneously in the 171 and 195 Å wave bands, during the time interval of 1998 February 17, 0215–0300 UT. Geometric parameters include the length and width of flare loops, which were derived from measurements of the ellipsoidal flare area under consideration of the area filling factor. We modeled the volume of the EUV-bright flare loop with a cylindrical, semicircular flare loop geometry and by correcting for EUV-dark loop segments below a chromospheric height of $h_{\mathrm{Ch}} = 2500$ km. Based on this geometric model we constrain the column depth h of EUV emission measures EM by the transverse width w of the flare loops (i.e., $h \approx w$), which is found to scale proportionally to the flare loop length. From the emission measure EM we then determined physical parameters such as the electron density, the pressure, and thermal energy content per flare. Then we studied the temperature and density evolution during some 20 flares and calculated the radiative and conductive cooling times, which were then compared with the observed decay times. Further we compared the physical parameters of EUV nanoflares with SXR microflares and HXR flares, studied their frequency distributions, and calculated their area-averaged energy flux, which was compared with coronal heating requirements. The conclusions of this study are as follows:

1. The geometric and physical parameters of EUV flares detected in the quiet Sun consistently follow scaling laws from larger flares observed in SXR and HXR downward to smaller energies. In reference to the largest observed flares with energies of $E \approx 10^{32}$ ergs, HXR and SXR flares can be detected down to the *microflare* range ($E \gtrsim 10^{26}$ ergs), while EUV flares can be seen down to the *nanoflare* range ($E \gtrsim 10^{24}$ ergs). EUV nanoflares are characterized by much smaller temperatures ($T_e \lesssim 2$ MK), lower densities ($n_e \lesssim 10^9$ cm^{-3}), and somewhat smaller spatial scales ($l = 2$–20 Mm). EUV nanoflares share other characteristic with larger flares, i.e., they exhibit plasma cooling during the flare peak, which causes a time delay of the peak emission in cooler EUV channels (e.g., 171 Å with respect to 195 Å). All these physical properties support the interpretation that EUV nanoflares represent miniature versions of larger flare processes.

2. EUV nanoflares exhibit a rapid heating phase (on timescales of a few minutes) and cooling times that are compatible with theoretically calculated radiative cooling times t_{rad}. However, the theoretically calculated conductive cooling times t_{cond} are significantly shorter (about a factor 30) and thus require either smaller temperature gradients between the flare loop top and footpoints or repetitive heating cycles with an occurrence time of a few minutes. Also the energy balance in microflares is indicative of smaller temperature gradients, which requires efficient heating of the chromospheric flare loop footpoints, e.g., by chromospheric evaporation.

3. The frequency distribution (or global occurrence rate) of EUV nanoflares, normalized to the solar surface, is found to scale as $N(E) \approx 10^{-46}(E/10^{24}\ \mathrm{ergs})^{-1.8}$ (s^{-1} cm^{-2} ergs^{-1}). If we extend this scaling law over the entire frequency range where flares have been observed, which spans 8 orders of magnitude, $E = 10^{24}$–10^{32} ergs, we find that it matches the frequency distribution of SXR transient brightenings (10^{27}–10^{29} ergs) and yields a reasonable estimate of the thermal energy of largest flares. The extrapolated thermal energy exceeds the nonthermal energy observed in HXR by a factor of ≈ 10 for small flares ($E_{\mathrm{th}} \approx 10^{30}$ ergs), and a factor of ≈ 3 for large flares ($E_{\mathrm{th}} \approx 3 \times 10^{32}$ ergs). In the nanoflare energy range (10^{24}–10^{26} ergs) we find disagreement with respect to previously determined frequency distributions (Krucker & Benz 1998; Parnell & Jupp 2000). We find that this disagreement is attributed to three effects: (1) the time-coincidence criterion in defining the spatial extent of flare events, (2) the discrimination of flarelike events from nonflaring EUV brightenings, and (3) the assumed value of the column depth in calculating the electron density in flare loops. We conclude that the value of the power-law slope in the frequency distribution of nanoflares critically depends on these three issues.

4. Investigating the question whether energetically smaller flare events (than currently detected down to an energy of $E_{\mathrm{th}} \approx 10^{24}$ ergs) could exist and possibly contribute to coronal heating, we find four physical limits. All four limits are based on extrapolating the scaling of physical parameters from larger flares to smaller flares. Using these scaling laws we find, below a thermal energy of $\lesssim 10^{24}$ ergs, that (1) the temperature drops below $\lesssim 1$ MK (implying *coronal cooling*), (2) the electron density drops below $\lesssim 10^8$ cm^{-3} (violating pressure balance), (3) the spatial size of flare

loops becomes smaller than the chromospheric height (absorption of EUV emission), and (4) the area coverage limit of 100% is reached at energies of $\approx 10^{21}$–10^{24} ergs. Based on these scaling laws, we conclude that there exists no meaningful extrapolation of physical parameters into the picoflare regime (below energies $\lesssim 10^{24}$ ergs).

5. The global (area-averaged) energy flux of EUV nanoflares in our observation amounts to $P \approx 10^3$ ergs s^{-1} cm^{-2}, which is a factor ≈ 300 below the coronal heating requirement for the quiet Sun, i.e., $P \approx 3 \times 10^5$ ergs s^{-1} cm^{-2} (Withbroe & Noyes 1977). If we average over all flare energies in the total energy range of $E_{\rm th} = 10^{24}$–10^{32} ergs, the total energy flux increases to $P \approx 2 \times 10^4$ ergs s^{-1} cm^{-2}, which is still a factor ≈ 15 below the coronal heating requirement. The results of this study further indicate that neither a power-law slope in excess of $a > 2$ for the frequency distribution nor an extrapolation of physical parameters to the picoflare regime is justified in the framework of this analysis.

The results of this study suggest the insufficiency of nanoflares (or picoflares) to heat the corona. We like to emphasize that this result is based on several assumptions made in the flare detection algorithm, the flare discrimination criterion, and in the physical models involved in calculating thermal energies and radiative losses in flares. We recommend that future studies further investigate these assumptions and quantify what systematic errors these assumptions introduce in the analysis of small flares. If the results hold up that the rate of detected nanoflares is insufficient to heat the corona, we have a *missing* (*luminous*) *mass problem*, which points to invisible energy carriers such as waves, magnetic fields, and electric currents.

Work on *TRACE* data was sponsored by NASA contract NAS 5-38099. We thank Arnold Benz and Säm Krucker for initiation of this study and critical and helpful comments during the analysis phase. We recognize the helpful *TRACE* planner duties of Ed DeLuca during the *TRACE* observations analyzed here. We acknowledge also helpful discussions, software support, and assistance in data processing from the *TRACE* team. The *TRACE* team includes scientists from Lockheed Martin Advanced Technology Center, Stanford University, NASA Goddard Space Flight Center, the University of Chicago, Montana State University, and the Harvard-Smithsonian Center for Astrophysics.

APPENDIX

TRACE RESPONSE FUNCTION

The instrumental response function of the *TRACE* 171 Å (Fe IX/X) and 195 Å (Fe XII) passband is shown in Figure 12, produced by the IDL procedure TRACE_T_RESP (written by Charles Kankelborg and Harry Warren) using the CHIANTI atomic line database (Dere et al. 1997), which contains some 1400 emission lines in the 150–400 Å wavelength range. The response function is publicly available in the Solar SoftWare (SSW) package (Freeland & Handy 1998), operating in IDL environment. The TRACE EUV response to a solar plasma at temperature T_e has a peak response at $T_{\rm peak} = 0.96$ MK at a wavelength of 171 Å , and peak response at $T_{\rm peak} = 1.37$ MK at a wavelength of 195 Å. The corresponding flux f_{171} (and f_{195}) in units of *data numbers* (DN) per pixel at the peak of the response function is

$$f_{171}(\mathrm{DN\ pixel^{-1}}) = 1.10 \times 10^{-26}(\mathrm{DN\ pixel^{-1}\ s^{-1}\ cm^5})\Delta t(\mathrm{s})\mathrm{EM}_{171}(\mathrm{cm^{-5}}) \quad \text{at } T_e = 0.96 \text{ MK}, \tag{A1}$$

$$f_{195}(\mathrm{DN\ pixel^{-1}}) = 0.81 \times 10^{-26}(\mathrm{DN\ pixel^{-1}\ s^{-1}\ cm^5})\Delta t(\mathrm{s})\ \mathrm{EM}_{195}(\mathrm{cm^{-5}}) \quad \text{at } T_e = 1.37 \text{ MK}, \tag{A2}$$

with $\mathrm{EM} = \int n_e^2(z)\,dz$ (cm^{-5}) being the emission measure integrated along the line of sight z. This new default calibration (status 1999 June) is calculated under the assumption of coronal elemental abundances (Feldman 1992) and the ionization

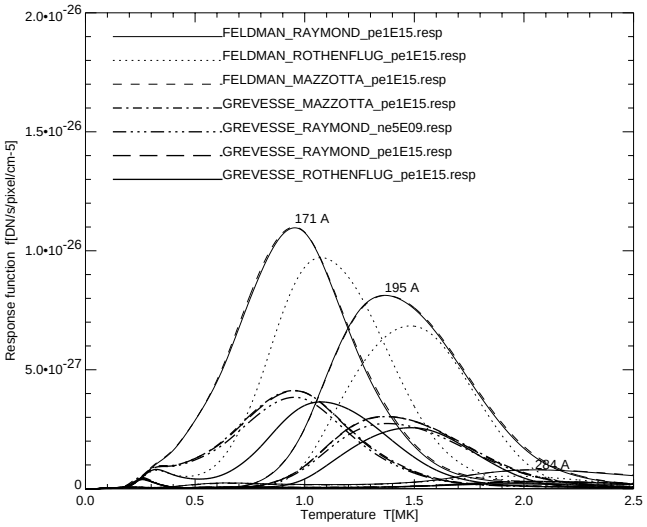

FIG. 12.—*TRACE* response function for the 171 and 195 Å wavelengths, calculated for two different abundances and three different ionization equilibria (see text in Appendix). The standard *TRACE* response function used as default in current SSW software refers to coronal abundances (highest curves with solid line style).

balance of Arnaud & Raymond (1992). The question arises whether coronal (Feldman 1992) or photospheric abundances (Meyer 1985) should be used for flare events. Both Feldman (1992) and Meyer (1985) account for the coronal *first ionization potential* (FIP) bias, but Meyer assumed that the low-FIP elements had photospheric abundances (and thus the high-FIP elements were depleted), while Feldman (1992) found that the low-FIP elements were overabundant with respect to the photosphere, while the high-FIP elements have photospheric abundances (see Fig. 2 in Feldman 1992). These coronal abundances lead to a 3.76 times higher emission measure than the photospheric abundances used earlier used by Meyer (1985) or Grevesse & Sauval (1998). The comparison of the coronal (Feldman 1992) versus photospheric (Grevesse & Sauval 1998) abundances is shown in Figure 12. Note that the 4 times higher response function leads, for a fixed observed flux, to a 4 times lower emission measure and thus to a $\sqrt{3.76} = 1.9$ times lower electron density, compared with earlier calibrations using photospheric abundances.

Figure 12 also illustrates different assumptions on three possible ionization equilibria (Mazzotta et al. 1998; Arnaud & Rothenflug 1985; Arnaud & Raymond 1992), calculated for a fixed pressure ($n_e \times T = 10^{15}$ cm^{-3} K) or for a fixed density $n_e = 10^9$ cm^{-3}. Calculations for a fixed density lead to a peak temperature that is about 10% higher, i.e., $T_{\rm peak} = 1.07$ MK versus 0.96 MK at 171 Å or $T_{\rm peak} = 1.48$ MK versus 1.37 MK at 195 Å.

REFERENCES

Arnaud, M., & Raymond, J. 1992, ApJ, 398, 394
Arnaud, M., & Rothenflug, R. 1985, A&AS, 60, 425
Aschwanden, M. J. 2000, Sol. Phys., in press
Aschwanden, M. J., & Benz, A. O. 1997, ApJ, 480, 825
Aschwanden, M. J., Nightingale, R. W., Tarbell, T. D., & Wolfson, C. J. 2000, ApJ, 535, 1027 (Paper I)
Benz, A. O., & Krucker, S. 1998, Sol. Phys., 182, 349
———. 1999, A&A, 341, 286
Berghmans, D., Clette, F., & Moses, D. 1998, A&A, 36, 1039
Biesecker, D. A., Ryan, J. M., & Fishman, G. J. 1994, in High-Energy Solar Phenomena—A New Era of Spacecraft Measurements, ed. J. M. Ryan & W. T. Vestrand (New York: AIP), 183
Cook, J. W., Cheng, C. C., Jacobs, V. L., & Antiochos, S. K. 1989, ApJ, 338, 1176
Crosby, N. B., Aschwanden, M. J., & Dennis, B. R. 1993, Sol. Phys., 143, 275
Culhane, J. L., et al. 1994, Sol. Phys., 153, 307
Dere, K. P., Bartoe, D. F., & Brueckner, G. E. 1989, Sol. Phys., 123, 41
Dere, K. P., Bartoe, D. F., Brueckner, G. E., Ewing, J., & Lund, P. 1991, J. Geophys. Res., 96, 399
Dere, K. P., Landi, E., Mason, H. E., Monsignori-Fossi, B. F., & Young, P. R. 1997, A&AS, 125, 149
Feldman, U. 1992, Phys. Scr., 46, 202
Feldman, U., Doschek, G. A., Behring, W. E., & Phillips, K. J. H. 1996, ApJ, 460, 1034
Freeland, S. L., & Handy, B. N. 1998, Sol. Phys., 182, 497
Grevesse, N., & Sauval, A. J. 1998, Space Sci. Rev., 85, 161
Handy, B. N., et al. 1999, Sol. Phys., 187, 229
Hudson, H. S. 1991, Sol. Phys., 133, 357
Krucker, S., & Benz, A. O. 1998, ApJ, 501, L213
Lin, R. P., Schwartz, R. A., Kane, S. R., Pelling, R. M., & Hurley, K. C. 1984, ApJ, 283, 421
Litvinenko, Y. E. 1999, ApJ, 515, 435
Martens, P. C. H., Kankelborg, C. C., & Berger, T. E. 2000, ApJ, in press
Mazzotta, P., Mazzitelli, G., Colafrancesco, S., & Vittorio, N. 1998, A&AS, 133, 403
McTiernan, J. M., Fisher, G. H., & Li, P. 1999, ApJ, 514, 472
Meyer, J. P. 1985, ApJS, 57, 173
Moses, D., Cook, J. W., Bartoe, J.-D. F., Brueckner, G., & Dere, K. P. 1994, ApJ, 430, 913
Nitta, N., & Yaji, K. 1997, ApJ, 484, 927
Parker, E. N. 1988, ApJ, 330, 474
Parnell, C. E., & Jupp, P. E. 2000, ApJ, 529, 554
Porter, J. G., Fontenla, J. M., & Simnett, G. M. 1995, ApJ, 438, 472
Porter, J. G., Moore, R. L., Reichmann, E. J., Engvold, O., & Harvey, K. L. 1987, ApJ, 323, 380
Rosner, R., Tucker, H., & Vaiana, G. S. 1978, ApJ, 220, 643
Shimizu, T. 1997, Ph.D. thesis, Natl. Astron. Obs., Mitaka, Tokyo, Japan
Shimizu, T., & Tsuneta, S. 1997, ApJ, 486, 1045
Shimizu, T., Tsuneta, S., Acton, L. W., Lemen, J. R., & Uchida, Y. 1992, PASJ, 44, L147
Sterling, A. C., Hudson, H. S., Lemen, J. R., & Zarro, D. A. 1997, ApJS, 110, 115
Sturrock, P. A. 1980, Solar Flares, A Monograph from Skylab Solar Workshop II (Boulder: Colorado Associated Univ. Press)
Vesecky, J. F., Antiochos, S. K., & Underwood, J. H. 1979, ApJ, 233, 987
Withbroe, G. L., & Noyes, R. W. 1977, ARA&A, 15, 363
Zirker, J. B. 1993, Sol. Phys., 148, 43